139 European Study Group with Industry

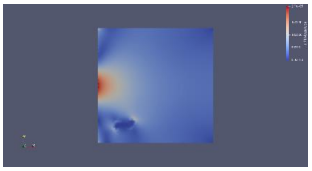
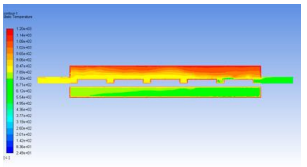
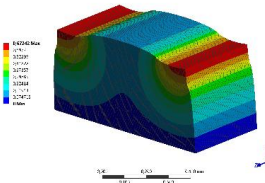
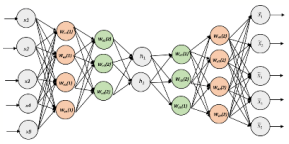
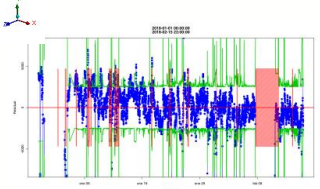

Laureano Escudero Bueno
Manuel Febrero Bande
Macarena Gómez Mármol
Andrés Prieto Aneiros
Javier Roca Pardiñas

Facultad de Matemáticas | Santiago de Compostela

July, 9-13, 2018

[math-in].net Red Española Matemática-Industria

ITMATI

MI-NET

cost EUROPEAN COOPERATION IN SCIENCE & TECHNOLOGY

COST is supported by the EU Framework Programme Horizon 2020

PROCEEDINGS OF THE

139 EUROPEAN STUDY GROUP WITH INDUSTRY (139 ESGI)

Santiago de Compostela, $9 - 13^{th}$ July, 2018

Editors

Laureano Escudero Bueno
University rey Juan Carlos
laureano.escudero@urjc.es

Manuel Febrero Bande
University of Santiago de Compostela
manuel.febrero@usc.es

Macarena Gómez Mármol
University of Sevilla
macarena@us.es

Andrés Prieto Aneiros
University of A Coruña
andres.prieto@udc.es

Javier Roca Pardiñas
University of Vigo
roca@uvigo.es

Printed by Spanish Network for Mathematics & Industry (math-in)

PROCEEDINGS OF THE

139 EUROPEAN STUDY GROUP WITH INDUSTRY (139 ESGI)

This volume contains the proceedings of the 139 European Study Group with Industry (139 ESGI) held in Santiago de Compostela, Spain, from 9th to 13th July 2018.

The 139 ESGI was jointly organized by the Technological Institute for Industrial Mathematics (ITMATI), the Spanish Network for Mathematics and Industry (math-in) and the COST Action TD1409, Mathematics for Industry Network (MI-NET).

The 139 ESGI was also co-funded by the Ministry of Economy, Industry and Competitiveness–State Research Agency with the nº of reference MTM2016-81745-REDT through the Thematic Network RTmath-in and via the Strategic Network in Mathematics with the nº of reference MTM2016-81711-REDE, granted within the call "Networks of Excellenc" 2016; by the Regional Ministry of Culture, Education and University Planning of the Regional Government of Galicia through the Technological Network of Industrial Mathematics (TMATI Network); by the agreement that ITMATI has with this Regional Ministry; and by ROMSOC project, financed by the EU within the Horizon 2020 Research and Innovation Programme under the Marie-Skłodowska-Curie grant agreement No 765374.

The 139 ESGI was also sponsored by the Faculty of Mathematics of the USC, which provided the rooms for holding the event.

Index

Introduction

Initiated in Oxford in 1968, Study Groups with Industry provide a forum for industrial scientists to work alongside academic mathematicians on problems of direct industrial relevance. They are an internationally recognized method of technology and knowledge transfer between academic mathematicians and industry, usually lasting one week.

The success of the ESGI lies in its unique format which has been copied around the world, and which allows Mathematicians to work on reduced groups to study problems presented by industry. These problems arise from any economic sector thanks to the versatility of Mathematics.

The objective is to present the capabilities of Mathematics and its applicability in a large part of the challenges and needs that industry presents. It aims to bring small, medium and large companies a technology with great potential, used by highly qualified researchers and which does not require large investments to use.

Therefore, collaboration between industry experts and researchers is key to address technological innovation issues by using successful mathematical techniques. ESGI contributes to the promotion of mathematics and helps companies to use Mathematics to improve their processes.

The goals which want to be reached at the ESGI are:

- find solutions and bring new insights to existing industrial problems;
- establish lasting and productive working relations between industry and mathematicians;
- propose new lines of research based on business challenges;
- reinforce the importance of mathematics in industry and mathematical profiles companies; and
- stimulate greater awareness of the power of mathematics to provide solve real-world problems.

Finally, it should be pointed out that 52 researchers, students, professors and company technicians contributed to a successful 139 ESGI.

Santiago de Compostela on 18th October, 2019

Members of the Scientific Committee:

- Laureano Escudero Bueno. Professor of Statistics and Operations Research. Rey Juan Carlos University. Member of the board of the Spanish Network for Mathematics and Industry (math-in).

- Manuel Febrero Bande. Professor of Statistics and Operations Research. University of Santiago de Compostela. Affiliated researcher of ITMATI.

- Macarena Gómez Mármol. Associate Professor in the Department of Differential Equations and Numerical Analysis. University of Seville (US). Member of the Spanish Network for Mathematics and Industry (math-in).

- Prieto Aneiros, Andrés. Associate Professor in the Department of Mathematics of the Faculty of Computer Science. University of A Coruña. Affiliated researcher to ITMATI.

- Roca Pardiñas, Javier. Associate Professor of Statistics and Operations Research. University of Vigo. Affiliated researcher of ITMATI.

Solidification and mechanical coupling in the propagation of microcracks

Academic Coordinator Marco Antonio Fontelos López
University Autonomous University of Madrid and CSIC-ICMAT

Business Coordinators Ángel Rivero Jiménez
Company Repsol Technology Center

Specialist Gerardo Enrique Olega Apadula
University Complutense University of Madrid

Team David Aller Giráldez (REPSOL), Pedro Fontán Muíños (REPSOL), Juan Carlos López Ríos (Yachay Tech, Ecuador), Jerónimo Rodríguez García (Universidade de Santiago de Compostela and ITMATI).

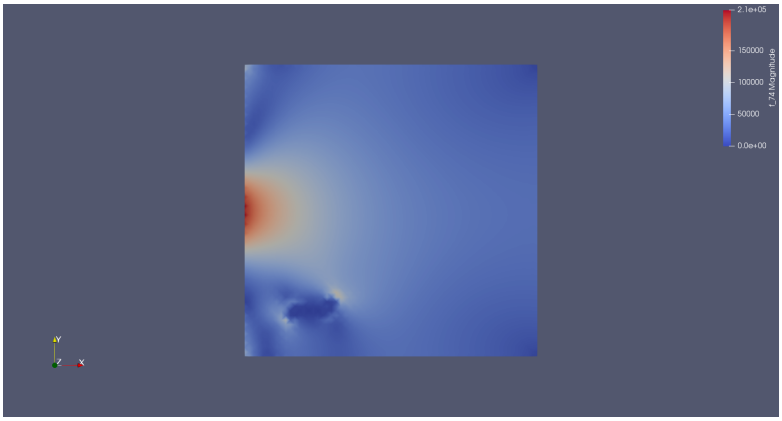

Solidification and mechanical coupling in the propagation of microcracks

David Aller Giráldez[1], Pedro Fontán Muíños[1], Marco Antonio Fontelos López[2], Juan Carlos López Ríos[3],

Gerardo Oleaga Apadula[4], Ángel Rivero Jiménez[5], Jerónimo Rodríguez García[6]

Abstract

We consider the formation and propagation of dendrites close to an electrode in a galvanic cell. We explain them as the result of edge effects in an electric field coupled with a local intensification of the flow of ions. A phase-field model has been developed for full numerical simulations of the problem. The dendrites produce a load on the solid electrolyte and may induce the growth of microcracks. Again, phase field models have been considered, discussed and implemented numerically so that growth of a crack can be observed provided the load is sufficiently large.

1. Introduction

A galvanic cell, or voltaic cell is an electrochemical cell that derives electrical energy from spontaneous redox reactions taking place within the cell. It consists of two different metals (electrodes) connected by a salt bridge. In certain classes of cells, positive ions can deposit on the electrode (anode)

[1] REPSOL
[2] Autonomous University of Madrid and CSIC-ICMAT; marco.fontelos@icmat.es
[3] Yachay Tech, Ecuador
[4] Complutense University of Madrid
[5] Repsol Technology Center
[6] University of Santiago de Compostela and ITMATI

itself making it grow. It has been observed that such a growth is sometimes uneven, giving rise to the spontaneous appearance of dendrites. The dendrites may grow up to several millimeters and produce an important load on the electrolyte. In cases when the electrolyte consists of a porous material or contains solid separators, this may lead to fracture, electric current flows through it and dielectric breakup or short-circuiting develops and destroys the whole device.

Our purpose is to use mathematical analysis, modelling and numerical simulation to understand two processes: the appearance of dendrites and the elastic fracture of the material induced by the dendrites. One of the main tools is the development of phase-field models. Such models were initially developed in the context of material science (cf. [1], [2] or the recent review [3]) in order to understand phase separation and coarsening phenomena, but now have extended to most areas in continuum mechanics and, in particular, to fluid mechanics when interfaces are present and to the propagation of cracks in an elastic material.

Nanocracks are generally called microcracks in serious literature about fracture. The cracks causing fracture, are truly in the nanometer dimensions. A nanocrack is any small area inside your material where your material does not stick together properly. Nanocracks might be "true" cracks like the cracks propagating into glass when it breaks, just much, much smaller, or an inclusion of something with not much strength, for example graphite in (cast) iron. Nanocracks thus are defects in the material and typically so small that they are not visible, not even in the most powerful optical microscopes at thousandfold magnification. Even if your microscope would be a hundred times better, magnifying things hundred-thousand times, you would have a hard time to see the nanocracks that make some steels more fracture prone than others. Unfortunately, there are a lot of reasons why materials should contain or develop nanocracks with different if small sizes, shapes and densities (number per cubic centimeters). What that means is that there are a lot of reasons why identical materials might show different fracture behavior.

2. The mathematical model

A simple electrolytic solutions consists of positive and negative ions (say Na^+ and Cl^-, for instance) with concentrations c_+ and c_- respectively. Conservation of mass yields the equations

$$\frac{\partial c_+}{\partial t} + \nabla \cdot \mathbf{J}_+ = 0 \tag{1}$$

$$\frac{\partial c_-}{\partial t} + \nabla \cdot \mathbf{J}_- = 0 \tag{2}$$

with fluxes

$$\begin{aligned} \mathbf{J}_+ &= \mu_+ c_+ \mathbf{E} - D_+ \nabla c_+ \\ \mathbf{J}_- &= -\mu_- c_- \mathbf{E} - D_- \nabla c_- \end{aligned}$$

We are assuming that positive and negative fluxes consist of: diffusion, with diffusion coefficient D_+ and D_- respectively, and drift by the electric field $\mathbf{E}$ with ion mobilities μ_+ and μ_- respectively. For simplicity, we also assume the ions' valency z=1. Diffusibilities and mobilities are related by Einstein's relation:

$$D = \mu k_B T$$

where k_B is Boltzmann's constant and T the absolute temperature. At the anode-electrolyte interface, we assume in our modelling that there is absorption of a fraction χ of positive ions arriving at the anode at a rate

$$\mathbf{J}_+ \cdot \mathbf{n} = j\chi c_+$$

Finally, Poisson's equation serves to determine the electric field:

$$-\nabla \cdot (\varepsilon \mathbf{E}) = c_+ - c_- \tag{3}$$

Since there is deposition of ions at the anode, the metallic electrode will start to grow with a velocity proportional to the deposition flux

$$\frac{d\mathbf{x}_\Gamma}{dt} \cdot \mathbf{n} = \frac{\Gamma}{\rho} j\chi c_+ \tag{4}$$

3. Phase field model

Phase field modelling essentially amounts to replacing a model with moving interfaces (with all the numerical and theoretical difficulties that implies) by a model in which no interfaces are present. In such a model, the media separated by the interface are labelled with a "phase function" φ such that $\varphi \simeq 1$ corresponds to one medium and $\varphi \simeq 0$ to the other. The function φ changes very quickly from one medium to the other, typically at length scales of order ϵ, so that a "sharp interface" is replaced by a "diffuse interface" of thickness ϵ. This, of course, has to be done in a mathematically consistent manner so that one recovers the sharp interface model as $\epsilon \to 0$. The starting point of the analysis consists on replacing interfacial energies which are proportional to the interfacial area, by the so-called Allen-Cahn (or Ginzburg-Landau) energy

$$F_\epsilon = \int_\Omega \left(\frac{\epsilon}{2} |\nabla \varphi|^2 + \frac{g(\varphi)}{\epsilon} \right)$$

with g being a double-well potential such as

$$g(\varphi) = \varphi^2(1-\varphi)^2$$

so that $F_\epsilon \to \gamma \text{Area}$ as $\epsilon \to 0$ (by a theorem of Modica and Mortola). In this manner, important quantities such as the normal vector to a sharp interface or a Dirac delta concentrated at the interface can be replaced by equivalent quantities in terms of φ :

$$\begin{aligned} \mathbf{n} &\simeq \frac{\nabla\varphi}{|\nabla\varphi|} \\ |\nabla\varphi| &\simeq \delta_\Gamma \end{aligned}$$

and material parameters which experience a jump across the interface can be written in terms of functions depending on φ that interpolate between values at both sides of the interface. In our case, a natural phase field model is then:

$$\frac{\partial c_+}{\partial t} + \nabla\cdot(\mu_+(\varphi)c_+\mathbf{E} - D_+(\varphi)\nabla c_+) = -j\chi c_+ |\nabla\varphi| - \eta(\varphi)c_+ \quad (5)$$

$$\frac{\partial c_-}{\partial t} + \nabla\cdot(-\mu_-(\varphi)c_-\mathbf{E} - D_-(\varphi)\nabla c_-) = -\eta(\varphi)c_- \quad (6)$$

$$\nabla\cdot(\varepsilon(\varphi)\mathbf{E}) = c_+ - c_- \quad (7)$$

$$\frac{\partial\varphi}{\partial t} + \frac{\Gamma}{\rho} j\chi c_+ |\nabla\varphi| = M\left(\epsilon\Delta\varphi - \frac{g'(\varphi)}{\epsilon}\right) \quad (8)$$

Equation (8) is Allen-Cahn equation for our model. The term $\eta(\varphi)c_\pm$ at the right hand side of (5) and (6) takes into account a possible absorption of ions at the bulk of the materials.

4. Dendrites

Let us consider now the problem in one dimension (say constant along the y direction). If we think of a quasi-stationary situation in which the fluxes remain constant over time, we will have

$$\begin{aligned} \mu_+c_+\mathbf{E} - D_+c_{+,x} &= -j\chi \\ -\mu_-c_-\mathbf{E} - D_-c_{-,x} &= 0 \end{aligned}$$

Assuming, in addition, local equilibrium of charges near the interface, we conclude a value of the electric field there

$$E_0 = \frac{j\chi}{2\mu_+c_+(0)}$$

If the interface grows uniformly, it will grow with a velocity

$$c_0 = \frac{\Gamma}{\rho} j\chi c_+(0)$$

Next we introduce transversal periodic perturbations along the y direction,

$$\delta x(y,t) = \delta_0 e^{iky+wt}$$

insert unknowns with this periodic dependence in (1)-(4) and linearize to obtain the dispersion relation

$$\omega\left(\omega + D_+ k^2\right) - \frac{\mu_+ E_0 c_+(0)(j\chi)^2}{2D_+}\frac{\Gamma}{\rho}k = 0$$

with a global maximum at $k_{\max}$ that corresponds to wavelength of the fastest growing perturbation

$$\lambda_{\max} = 2^{\frac{4}{3}}\pi\frac{D_+}{j\chi}\left(\frac{4\rho}{c_+(0)\Gamma}\right)^{\frac{1}{3}}$$

Introducing typical values of the physical parameters in an electrolytic device such as a battery, we obtain $\lambda_{\max}$ ~10-100 μm which is consistent with the observed experimental values. The mechanism of formation of dendrites is the result of the destabilizing effect of the electric field: a local perturbation of the otherwise flat interface induced a local intensification of the electric field by the edge effect, this electric field produced an increase of the amount of ions drifted towards the interface which grows locally faster and this induces an even larger electric field. Only diffusion is able to stabilize the growth process a bit and, as a result, a typical wavelength balancing destabilizing and stabilizing effect appears.

5. Phase field formulation of the crack problem

5.1. General concepts

Phase field models have been introduced in the modelling of crack propagation by several authors (cf. [4], [5]). The main idea is to decompose the free energy in two terms:

$$\mathcal{F} = \mathcal{F}_{\text{surf}} + \mathcal{F}_{\text{el}}$$

that is, the elastic free energy (stored in the body) and the crack surface energy (dissipated through broken bonds).

The surface energy is connected to the length of the growing crack:

$$\mathcal{F}_{\text{surf}} = \gamma\Gamma$$

where γ is a coefficient related to crack energy per unit length of growth.

The elastic field displacement is u_i and the strain tensor:

$$\varepsilon_{ij} = \frac{1}{2}\left(u_{i,j} + u_{j,i}\right) .$$

Being C_{ijkl} the components of the elastic stress tensor, the expression of the elastic energy density in terms of the strain tensor is given by:

$$f_{\text{el}} = \frac{1}{2} C_{ijkl}\varepsilon_{ij}\varepsilon_{kl} \equiv \frac{1}{2}\sigma_{ij}\varepsilon_{ij},$$

so

$$\mathcal{F}_{\text{el}} = \int f_{\text{el}} \mathrm{d}x$$

The phase field is defined as:

$$\phi{=}1 \rightarrow \text{"healthy" material}, \quad \phi = 0 \rightarrow \text{cracked material} \quad 0 \leq \phi \leq 1$$

The main idea is to relax the elastic constants in the presence of cracks, in such a way that:

$$C^{\phi}_{ijkl} = g(\phi) C_{ijkl}$$

so that $g\left(0\right) = 0$, or at least, a very small value to avoid numerical instabilities, and $g\left(1\right) = 1$ so that the elastic properties are unaltered in the healthy material. A choice for g is given by:

$$g\left(\phi\right) = 4\phi^3 - 3\phi^4$$

The general formulation is independent of the particular choice of g.

Consider now the elastic energy variation associated to the change of the phase field. We must take care of two sources: the intrinsic change of the elastic constants, and the change of the equilibrium displacement field:

$$u^{\phi}_i \rightarrow \text{displacement field for a given } \phi$$
$$\varepsilon^{\phi}_{i,j} \rightarrow \text{strain tensor for given } \phi$$

That is

$$\varepsilon^{\phi}_{i,j} = \frac{1}{2}\left(u^{\phi}_{i,j} + u^{\phi}_{j,i}\right)$$

The stress field taking into account the phase field is given by:

$$\sigma^{\phi}_{ij} = C^{\phi}_{ijkl}\varepsilon^{\phi}_{kl}$$

and the equilibrium of the stress field (in the absence of body forces) is:

$$\sigma^{\phi}_{ij,j} = 0$$

Boundary conditions are imposed on displacements or stress, but independent of ϕ.

5.2. Variation of elastic free energy

$$\delta\mathcal{F}_{\text{el}} = \frac{1}{2}\int \delta\left(\sigma_{ij}^{\phi}\varepsilon_{ij}^{\phi}\right)\mathrm{d}x = \int \delta\left(g(\phi)C_{ijkl}\varepsilon_{ij}^{\phi}\varepsilon_{kl}^{\phi}\right)\mathrm{d}x$$
$$= \frac{1}{2}\int \left(g'(\phi)\delta\phi\sigma_{ij}^{\phi}\varepsilon_{ij}^{\phi} + 2g\left(\phi\right)C_{ijkl}\varepsilon_{ij}^{\phi}\delta\varepsilon_{kl}^{\phi}\right)\mathrm{d}x$$

(we used the symmetry properties of C, that is: $C_{ijkl} = C_{klij} = C_{jikl} = C_{ijlk}$). Rewriting:

$$\delta\mathcal{F}_{\text{el}} = \int g'(\phi)\delta\phi f_{\text{el}}\left(x\right)\mathrm{d}x + \int \sigma_{kl}^{\phi}\delta\varepsilon_{kl}^{\phi}\mathrm{d}x$$

where

$$f_{\text{el}}^{\phi} = C_{ijkl}\varepsilon_{ij}^{\phi}\varepsilon_{kl}^{\phi}$$

now taking into account that:

$$\int \sigma_{kl}^{\phi}\delta\varepsilon_{kl}^{\phi}\mathrm{d}x \equiv \int \sigma_{kl}^{\phi}\delta u_{k,l}^{\phi}\mathrm{d}x$$
$$= -\int \underbrace{\sigma_{kl,l}^{\phi}}_{=0}\delta u_{k}^{\phi}\mathrm{d}x + \text{boundary terms}$$

We have that:

$$\delta\mathcal{F}_{\text{el}} = \int g'(\phi)f_{\text{el}}^{\phi}\left(x\right)\delta\phi\left(x\right)\mathrm{d}x$$

or

$$\frac{\delta\mathcal{F}_{\text{el}}}{\delta\phi}[\phi] = g'(\phi\left(x\right))f_{\text{el}}^{\phi}\left(x\right)$$

It is noticeable that the variation depends only on the local rate of change of the elastic constants.

5.3. Phase field formulation of the crack length

To gain some intuition on how to capture the crack length, we consider the following 1-D example. Fix a "length scale" l. We consider a crack as a point where $\phi = 0$. The "measure" of this point in $\mathbb{R}$ is equal to 1, but we consider a fuzzy region surrounding this point, with length scale given by l. To fix ideas, consider:

$$\phi\left(x\right) = 1 - e^{-|x|/l_c}$$

with a "crack" in $x = 0$.

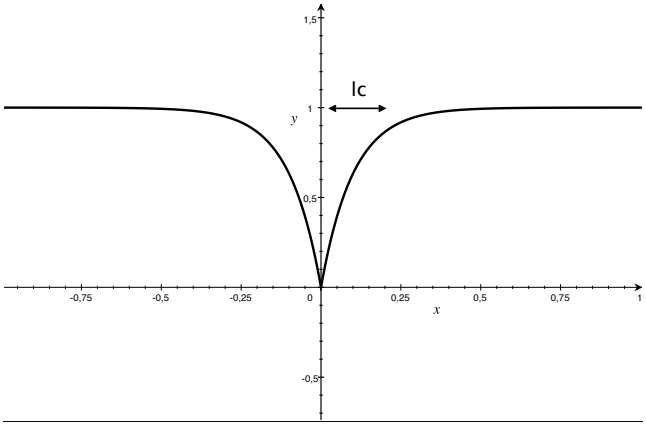

Figure 1: The one dimensional crack

This function solves the differential equation

$$l_c^2\phi'' - \phi = -1$$

And satisfies the variational principle:

$$\delta I = 0 \quad I[\phi] = \int_{-\infty}^{\infty} \left(l_c^2 \frac{(\phi')^2}{2} + \frac{(1-\phi)^2}{2} \right) dx$$

and for the minimum, the value of the functional is:

$$I[1 - e^{-|x|/l_c}] = l_c$$

so

$$\min_{\phi(0)=0} \frac{I[\phi]}{l_c} = 1$$

gives the "length" or linear measure of the crack in 1-D.

The general setting is:

$$I[\phi] = \int l_c \frac{|\nabla\phi|^2}{2} + \frac{(1-\phi)^2}{2l_c} \approx \text{length of the interface between } \phi = 0 \text{ and } \phi = 1.$$

The variation of I, after integration by parts is given by:

$$\delta I[\phi] = \int \left(-l_c \Delta\phi - \frac{1-\phi}{l_c} \right) \delta\phi \approx \delta\text{length of crack extension}$$

5.4. Phase fields and evolution

The general formula for crack evolution can be now stated. Consider the variation of the free energy obtained through a virtual extension of the phase field $\delta\phi$:

$$\begin{aligned}\delta\mathcal{F} &= \delta\mathcal{F}_{\text{surf}} + \delta\mathcal{F}_{\text{el}} \\ &= \int \left(\underbrace{\gamma\left(-l_c\Delta\phi + \frac{1}{l_c}V'(\phi)\right)}_{\text{length}} + \underbrace{g'(\phi)f_{\text{el}}^{\phi}(x)}_{\text{elastic}} \right) \delta\phi dx\end{aligned}$$

where:

$$V(\phi) = (1-\phi)^2$$

and, in the isotropic, homogeneous case:

$$f_{\text{el}}^{\phi}(x) := \frac{\lambda}{2}\varepsilon_{ii}^{\phi} + \mu\varepsilon_{ij}^{\phi}\varepsilon_{ij}^{\phi}$$

Now think of t as an artificial time measure, such that

$$\delta\phi = \phi_t dt$$

The idea is to select ϕ_t in the direction of the *gradient flow*, or maximum dissipation direction (Model 0):

$$\phi_t = -\frac{\delta\mathcal{F}}{\delta\phi} \equiv M\left(\gamma\left(l_c\Delta\phi - \frac{1}{l_c}V'(\phi)\right) - g'(\phi)f_{el}^{\phi}(x)\right)$$

with M a constant that can be absorbed as time scaling.

5.5. Problems

V: One or two potential wells?

Henry [4], [5] formulation: $V(\phi) = \phi^2(1-\phi)^2$, $g(\phi) = 4\phi^3 - 3\phi^4$.

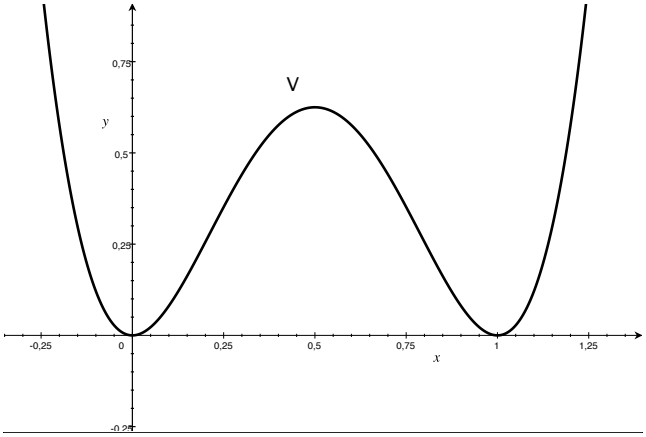

Figure 2: Double well potential

There is *no initialization* of a crack in a healthy region (for short times) even for high energy concentrations. If $\phi \equiv 1$ in some zone, then $V'(1) = 0$, and $g'(1) = 0$, then

$$\phi_t = 0$$

There is no need for a double well formulation. The length of the crack can be reproduced using a one-well energy. They add an "activation elastic energy" that proves to be useful to avoid spurious crack creation:

$$\mathcal{F}_{\text{el}} = g(\phi)(f_{\text{el}} - f_{\text{a}})$$

The activation energy *does not alter the elastic field equilibrium*, it only activates the crack if $f_{\text{el}} > f_{\text{a}}$.

One potential well (Kuhn-Müller [6]): $V(\phi) = (1-\phi)^2$, $g(\phi) = \phi^2$. There is initialization (not desired!). Consider a zone with $\phi \equiv 1$, now $V'(1) = 0$ but $g'(1) > 0$, then

$$\phi' = -g'(1) f_{\text{el}}$$

The healing problem

There is another, undesirable, aspect of the model. It allows the healing of a damaged zone, due to the fact that the evolution equation has reversibility. Consider a damaged zone with $\phi = c < 1$, constant in a ball. Then $\Delta\phi = 0$, $V'(c) < 0$ and $g'(c) > 0$, so, using Model 0:

$$\phi_t = M\left(-\frac{\gamma}{l_c}V'(\phi) - g'(\phi)\underbrace{f_{\text{el}}^{\phi}(x)}_{\approx 0}\right)$$

so, for a very low density of elastic energy, we will have that $\phi_t > 0$ and then the zone will be healed. This problem is removed by stating the non-reversibility

of crack damaged zone:

$$\phi_t = -\max\left(\frac{\delta F}{\delta \phi}, 0\right) \leq 0 \quad \text{(always decreasing)}$$

Other problems

The behavior of the cracked elastic field may differ a lot when the zone is under tension, but will not change when it is under compression. One way to deal with this problem is to separate two cases:

$$f_{\text{el}} = g(\phi) f_{\text{el}}^{+} + f_{\text{el}}^{-}$$

where f_{el}^{-} is activated when $\text{tr}\varepsilon < 0$ and f_{el}^{+} for $\text{tr}\varepsilon < 0$. Notice that, for $\phi = 1$ we have the full elastic (non damaged material) energy. For $\phi = 0$ only f_{el}^{-} is activated.

Our model

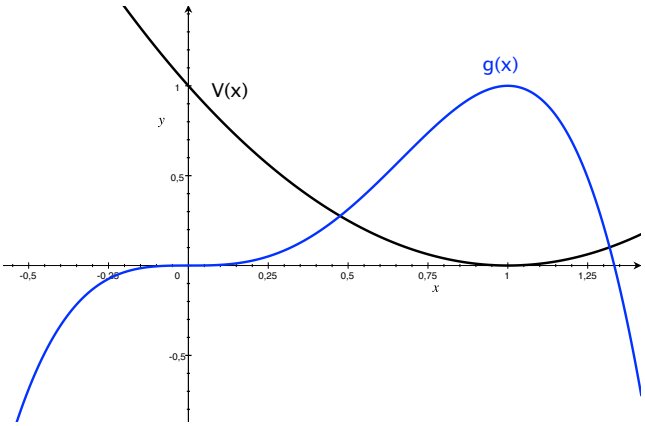

Figure 3: V and g

We take advantage of the simplicity of the single well potential, and a g function such that $g(0) = 0$, $g(1) = 1$ and $g'(1) = 0$. Also, we incorporate an *activation energy* f_{a}. So, we propose the problem:

$$\begin{cases} \sigma_{ij,j} = 0 \\ \phi_t = \min\left(M\left(\gamma\left(l_c \Delta\phi - \frac{1}{l_c} V'(\phi)\right) - g'(\phi)\left(f_{\text{el}}\left(\varepsilon^{\phi}\right) - f_{\text{a}}\right)\right), 0\right) \end{cases}$$

with

$$g(\phi) = 4\phi^3 - 3\phi^4$$
$$V(\phi) = (1-\phi)^2$$

We have the following properties:

1. Crack initiation is not possible in healthy materials. We have to induce random sites with a value $\phi \lessapprox 1$.
2. For sites with $f_{\text{el}}^{\phi} > f_{\text{a}}$ and $\phi < 1$, activation is possible. If ϕ is approximately constant, then $V'(\phi) > 0$ and then the right hand side is strictly negative.
3. Healing is not possible.

6. Numerical treatment

Using finite differences it would be straightforward to implement an explicit scheme:

1. Given ϕ_n, u_n at some time step, estimate the right hand side at each node:

$$\theta = M\left(\gamma\left(l_c\Delta\phi_n - \frac{1}{l_c}V'(\phi_n)\right) - g'(\phi_n)\left(f_{\text{el}}\left(\varepsilon^{\phi_n}\right) - f_{\text{a}}\right)\right)$$

   if it is positive at some point, then $\phi_{n+1} = \phi_n$, if it is negative, then: $\phi_{n+1} = \phi_n + \theta\Delta t$. This computation is *local*, it must be performed for each $x \in \Omega$.
2. Update the elastic field for the new ϕ_{n+1} (so, new elastic constants).
3. Repeat.

Using a variational formulation we can integrate by parts the first term, giving a weak form for tests functions q:

$$\int \phi_t q = M\int \gamma\left(-l_c\nabla\phi_n\nabla q - \frac{1}{l_c}V'(\phi_n)\,q\right) + g'(\phi_n)\left(f_{\text{el}}\left(\varepsilon^{\phi_n}\right) - f_{\text{a}}\right)q$$

Using a set of basis functions $\phi = \sum c_i e_i$, $\phi' = \sum c_i' e_i$ solving the linear problem, we obtain a system of odes. After solving for one time step, we can impose the non-healing condition:

$$\phi_{n+1}^{\text{corrected}} = \min\left(\phi_{n+1}^{\text{predictor}}, \phi_n\right).$$

The results of solving the model numerically can be seen in figures (4)-(7). A point load (representing a dendrite that is growing) has been applied at the right hand side of a square and a pre-crack has been created artificially at some

distance. As can be seen from the figures, stress accumulates at the tips of the crack and the result is its growth when the load exceeds a certain limit.

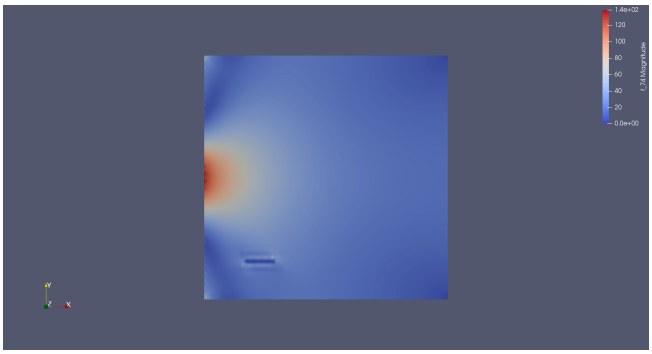

Figure 4: Initial stress field. A point load is placed at the left hand side and a small initial crack at the bulk.

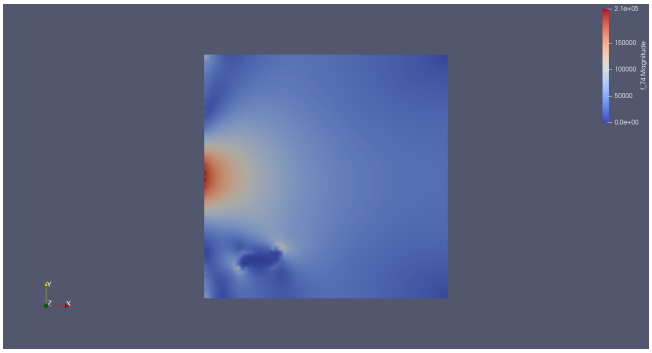

Figure 5: Final stress field. Notice the accumulation of stress at the tips of the crack and its growth and propagation.

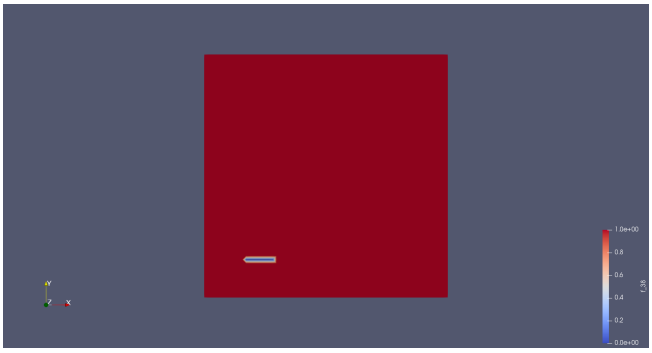

Figure 6: Initial phase field.

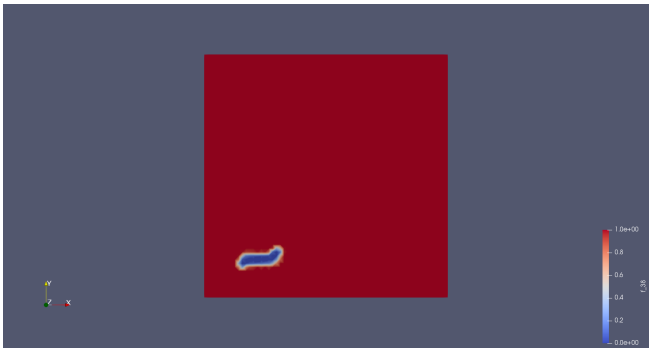

Figure 7: Final phase field. Notice that the crack has grown and propagated.

References

[1] S. M. Allen and J. W. Cahn, Ground State Structures in Ordered, Binary Alloys with Second Neighbor Interactions, Acta Metall. 20, 423 (1972).

[2] J. W. Cahn and J. E. Hilliard, Free energy of a nonuniform system I., Interfacial free energy, J. Chem. Phys. 28, 258 (1958).

[3] W. J. Boettinger, J. A. Warren, C. Beckermann, and A. Karma, Phase-Field Simulation of Solidification, Annual Review of Materials Research, Vol. 32 (2002),163-194.

[4] H. Henry, Study of three-dimensional crack fronts under plane stress using a phase field model, EPL, 92 (2010) 46002.

[5] H. Henry, Study of the branching instability using a phase field model of inplane crack propagation, EPL, 83 (2008) 16004

[6] C. Kuhn, R. Müller, A continuum phase field model for fracture, Engineering Fracture Mechanics 77(18) (2010), 3625-3634.

Simplified Modeling of Brazing Furnaces

Academic Coordinator Elena Martín Ortega
University University of Vigo and Technological Institute for Industrial Mathematics (ITMATI)

Business Coordinators Anxo Feijóo Lorenzo and Jose Carlos Pérez Ramillo
Companys Ecomanagement Technology and BorgWarner

Specialist Fernando Varas Mérida
University Technical University of Madrid (UPM)

Team Ashwin Sadanand Nayak (University of A Coruña and ITMATI), Hayley Wragg (University of Bath), Youssef Fathallah (University of Santiago de Compostela), Mª Dolores Gómez Pedreira, José Luis Ferrín González (University of Santiago de Compostela and ITMATI), Nerea Vilela Barreira and Damián Bazarra Castro (EcoMT) and Carlos Coroas Fombella (University of Vigo)

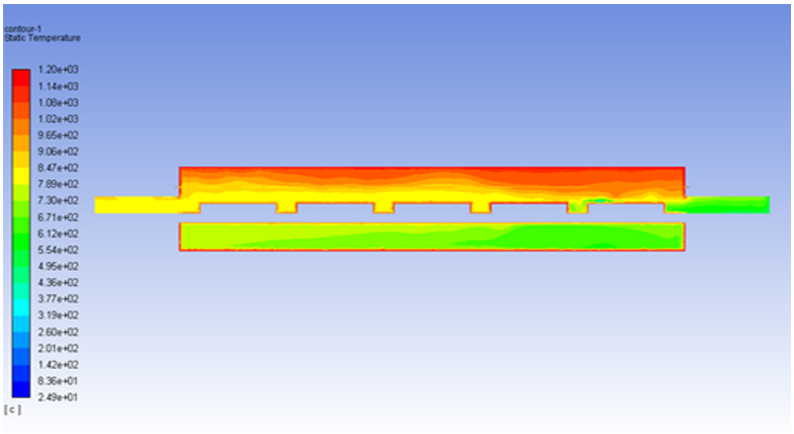

Simplified Modeling of Brazing Furnaces

E. Martín[1], A. S. Nayak[2] and F. Varas[3]

Abstract

This work tackles different modeling approaches to describe the brazing process of automotive stainless steel pieces inside continuous furnaces with controlled (reducing) atmosphere. In particular, three different models, which are complementary between them, are described. The first one, a global zone model, describes the mass flow exchanges and simplified energy balances between the different zones present in this type of furnaces. The second one is a (more) detailed zone model, where each zone is decomposed in various sub-zones (control volumes) for which different energy balances (for the gases, pieces and furnace walls) and mass conservation equations of gaseous species (H_2 and H_2O) are imposed. Finally, the third method presented consists on a CFD numerical model of the muffle region of the furnace. After the necessary validation process, these approaches can lead to a good understanding of the thermal conditions and local atmosphere present inside the different regions of the furnace and can potentially be used to predict the effects caused by any change in an operational parameter (e.g. the mass flow injection of H_2, injection location, conveyor velocity, ...) of the furnace. However, prediction of the quality of the brazing process along specific regions of the pieces would require much more detailed models that are out of the scope of this work.

[1] University of Vigo and ITMATI; emortega@uvigo.es
[2] University of Coruña; ashwin.nayak@udc.es
[3] Technical University of Madrid (UPM); fernando.varas@upm.es

1. Introduction to the brazing process

The use of controlled atmosphere continuous furnaces for brazing of stainless steel pieces is increasing with rising demand of stainless steel parts by manufacturers of aerospace and automotive industries.

The brazing process (see [1] for a complete reference) is a joining manufacturing process between metal parts that uses a filling metal (paste, ring or foils of copper alloy, nickel-chromium-boron alloys etc.). The filling is deposited on the metal junction and the set is then submitted to a high temperature in a furnace in order to melt the filling material. By capillary effect on the walls of the narrow gap between the parts to be joined, the filling enters the junction and a metal alloy is formed in the process of solidification and, consequently, the metals pieces are joined, as described in figure 1. The filler metal must have a lower melting temperature than the materials it is joining and must be of a similar base to them.

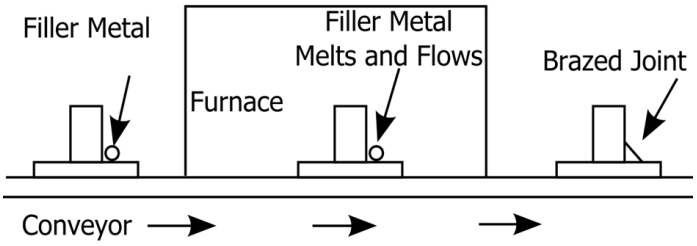

Figure 1: Simplified diagram of the brazing process.

The key to a successful brazing is the preparation of the surface. Contaminant elements and metal oxides prevent the filler metal from forming an alloy with the metals of the parts to be processed. Also, in case of little oxidation, the pores of the surface to be processed will be closed by the oxide, preventing the capillary action and the brazing itself. This is why the furnace atmosphere needs to be reducing in the brazing process and maintained so in a controlled fashion. Keeping the surface of the parts in the furnace reduced is much more difficult for brazing of stainless steel parts than for brazing of mild steel parts. In particular, the chromium in the stainless steel creates a much more stable oxide at an oxygen level much lower than that of carbon steel.

The oxide on the surface must be reduced before reaching the melting temperature of the filler. Usually this reduction is made through a reaction of hydrogen with the oxygen present in the metal oxide, forming water vapor (1).

$$M_xO_y + yH_2 \underset{b}{\overset{f}{\rightleftarrows}} xM + yH_2O \tag{1}$$

Too much water vapor (or oxygen) in the system prevent the reaction from continuing and, therefore, from reducing the oxide. To determine the water

vapor levels inside the furnace atmosphere the dew point is used. The dew point is the temperature at which a quantity of water vapor in the system saturates the atmosphere and condenses, forming little water drops. Usually the dew point required for brazing of stainless steel junctions in a high concentration hydrogen atmosphere is very low, which requires very high furnace temperatures at the brazing zone [1]. As an example, for AISI 300 series stainless steel, the required dew point is $-50°C$ and the brazing temperature is usually between 1040 and 1100°C in atmosphere with high concentration of hydrogen ($\sim$ 75-80%) if the brazing is performed with copper or nickel-chromium–phosphorus, and pure hydrogen (100%) if nickel-chromium-boron filler or silicon are used.

The continuous furnace with controlled atmosphere is the economically best way for brazing of high quantity of pieces in stainless steel. An sketch of a typical brazing furnace and its main regions is shown in figure 2 along with their corresponding temperature-time diagram.

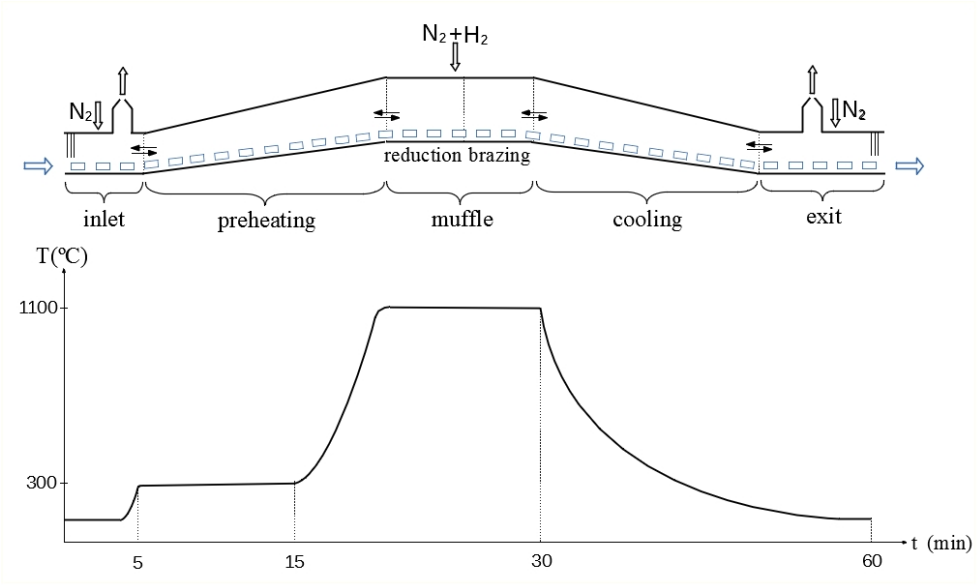

Figure 2: Sketch of a continuous brazing furnace and its common parts: pieces inlet (with curtain), inlet hood, preheating zone, muffle, cooling zone, outlet hood, and pieces outlet (with curtain).

The temperature–time relation is the first step to achieve a good product quality. The thermal energy provided by the furnace is used for different functions. The part to be processed has to be heated first at a temperature at which the surface oxide of the base metal can be reduced as a result of the reaction of the present iron oxides and the reducing components of the controlled atmosphere. Extra energy is necessary to melt the filler metal and form an alloy with the base metal. As for copper and AISI 300 series stainless

steel, the variation of the temperature for the brazing is between $1090-1100°C$ and for nickel-chromium alloys it is between $1080-1130°C$. This temperature depends on the shape and composition of the brazing metal, on the type of component and its assembly, as well as on other operating conditions, such as speed of the conveyor belt or the length of the heating zone.

The local reducing atmosphere present at the muffle zone is fundamental to achieve a correct brazing. Therefore, the optimal configuration implies working with a furnace in positive operation pressure to avoid air infiltration inside the furnace. Taking into account the high cost of H_2, controlling the efficiency of the furnace is vital. Thus, information concerning the flow along the doors as well as internal flows between different parts of the furnaces and its dependency with other operational conditions (atmospheric humidity and pressure inside the plant, H_2 mass flow injection, ...) is crucial.

2. Simplified Modeling

ECOMT[1](A Coruña, Spain) is a leading company in monitoring data for different productive industrial processes to control and improve the energy efficiency of different installations. As a demand to improve the efficiency of the brazing process for their client BorgWarner Emissions Systems Spain S.L.[2] (Vigo, Spain), a leading industry provider of automotive parts, the team centered its objective in designing the steps needed for developing a "digital twin" of the furnace which responds like a real furnace installed in the client company (see figure 3)

Figure 3: Example of arrangement of the pieces on the conveyor at the furnace inlet (left) and picture of a complete furnace line (right) installed at Borgwarner Emissions Systems Spain S.L. Company.

The final model aims to give an insight on the real distribution of the

[1] https://ecomt.net
[2] https://www.borgwarner.com/company/locations/vigo

reducing atmosphere inside the furnace and its dependence on the injected hydrogen mass flow.

2.1. Global Zone Model

The global zone model tries to capture the mean values of the flow properties for each one of the six zones of the furnaces (as indicated in figure 2): inlet, preheating, reduction and brazing sections of the muffle, cooling and exit zones. For each zone, balances of mass flow for each species and energy should be solved. Therefore, the variables considered for the global zone model would be

- Averaged temperature for each zone
- Averaged concentration of H_2 and H_2O for each zone
- Averaged working piece temperature at each piece position
- Concentration of trapped H_2O inside each piece at each piece position

The last variable is relevant for the brazing process as it is has been observed that the dew point inside the muffle is sensible to the local atmospheric conditions in the plant. Thus, the kinetics of the reduction/oxidation reaction is affected by this parameter and, consequently, the final quality of the brazing.

A direct approach to obtain the total mass flow exchanged between zones would be to solve a simple hydraulic network that allows to relate mass flows to differences of pressure between the regions. Once the total mass flows are obtained, the next step would be to solve the energy balance and the distribution of the mass flow between the three different gases H_2, H_2O and N_2 for each zone. Some of the parameters included in this model (e.g. the parameters needed to configure the head losses in the hydraulic network) would need calibration through sensors and experimental measurements extracted from the industrial furnace.

Results of this model can be satisfactory when applied to certain control tasks. However, the global model cannot retain all the details needed to ensure a correct brazing process. As the model only deals with averaged temperature and concentrations of H_2 and H_2O inside each zone, the information provided by the model is clearly insufficient to relate to the quality of the brazing.

Therefore, more complicated models are presented below. The first one, a detailed (and more accurate) zone model, is presented in the next section 2.2. The second one, a computational fluid dynamics (CFD) model of the muffle region, which uses (partially) some information extracted from the global zone mode, will be described in section 2.3. Likewise, some information post-processed from the CFD model can be used as inputs in the detailed zone model, as we will see later.

2.2. Detailed Zone Model

This model considers each of the six different zones (or at least the muffle region) divided into N number of different control volumes (depending on the level of details aimed to be retained) as in figure 4. For each control volume, energy balances are solved, having the same variables as in the global zone model but extended along each control volume. To determine the exchange of H_2 and H_2O mass flows between adjacent control volumes ($\dot{m}_{i,i'}$ in the equations that follow), conservation balances of mass and momentum should be imposed. Unfortunately, this approach is not precise enough to characterize the flows, due to the complex mechanisms involved in the thermal-fluid dynamic problem. Instead, a more accurate approach would be to approximate these fluxes with the results from the CFD model, post-processed for each control volume. Also, additional parameters involved in the detailed zone model should be modeled numerically or, alternatively, estimated experimentally.

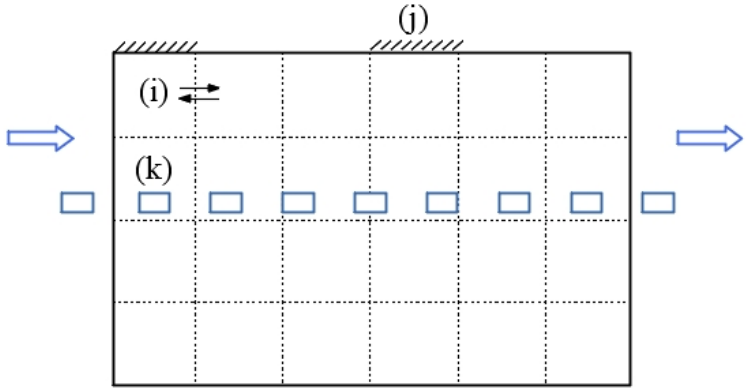

Figure 4: Sketch of the different control volumes in the muffle region.

Thus, a model with N control volumes ($i = 1, 2, ..., N$), a total number S_w of solid surfaces over the furnace walls ($j = 1, 2, ..., S_w$) and a total of K different pieces positions ($k = 1, 2, ..., K$) is then considered. Each energy and mass flow balance will be explained as follows.

2.2.1 Energy balance at each control volume

Following the work of Tan et al. [2], the energy balance for the i–th control volume (see figure 5) can be expressed by the following equation (2), assuming

a steady temperature for the gases and the furnace walls:

$$\sum_{\substack{i'=1,\\ i\neq i'}}^{N} \overleftarrow{G_i G_{i'}}\ \sigma T^4_{vc(i')} + \sum_{j=1}^{S_w} G_i S_j \sigma T^4_{wall(j)} + \sum_{k=1}^{K} G_i \hat{S}_k \sigma T^4_{wp(k)} - a V_i \sigma T^4_{vc(i)} -$$

$$- \sum_{\substack{interfaces,\\ (i)-(i'')}} c_p{}^g \dot{m}_{i,i"} T_{ve(\substack{upwind\\ i,i"})} - \sum_{\substack{working\ pieces\ in\\ control\ volume(k)}} c_p^{wp}\ \frac{m_{wp}}{t_{res}} (T_{wp(k)} - T_{wp(k-1)}) = 0 \quad (2)$$

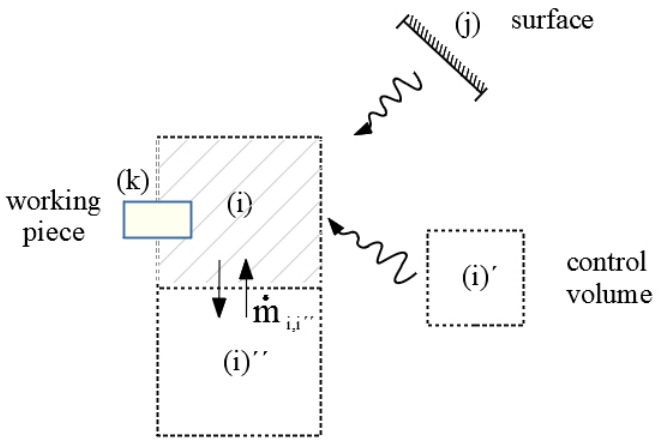

Figure 5: Sketch of the different interactions that take place in the energy balance inside a control volume.

The first three terms account for the thermal radiation that the gas receives from the gas inside the other zones, from the furnace walls and from the pieces, respectively. The fourth term takes into account the thermal radiation emitted from the gas in the i–th control volume. The fifth term accounts for the convective heat transport between control volumes, while the last term represents the enthalpy variation of the pieces that cross the control volume.

2.2.2 Energy balance on each work piece

This balance represents the enthalpy variation of the pieces as they move across the furnace. The pieces heating or cooling will be the result of the right hand term of equation (3), which takes into account, respectively, the radiation coming from the furnace walls, radiation coming from the gas of different control volumes and from other positions, the heat exchanged with the gases and the thermal radiation emitted by the piece in this position k (see figure

6):

$$c_p{}^{wp}\ \frac{m_{wp}}{t_{res}}(T_{wp(k)} - T_{wp(k-1)}) = \sum_{j'=1}^{S_w} \overleftarrow{\hat{S}_k S_{j'}}\ \sigma T^4_{wall(j')} + \sum_{i'=1}^{N} \overleftarrow{\hat{S}_k G_{i'}}\ \sigma T^4_{cv(i')} +$$
$$+ \sum_{\substack{k'=1,\\ k'\neq k}}^{K} \overleftarrow{\hat{S}_k \hat{S}_{k'}}\ \sigma T^4_{wp(k')} + \hat{A}_k h_k (T_{vc(i)} - T_{wp(k)}) - \hat{A}_k \epsilon_k \sigma T^4_{wp(i)} \quad (3)$$

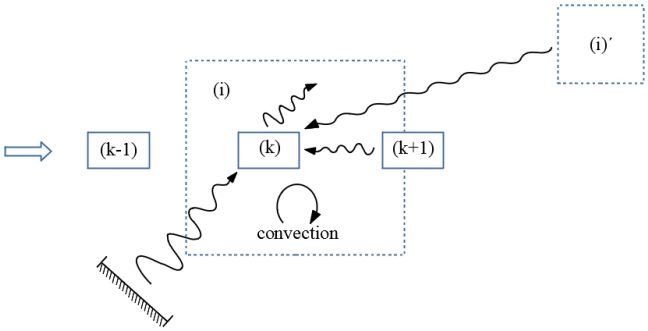

Figure 6: Interactions in the energy balance for each piece

2.2.3 Energy balance on wall surfaces

The following equation (4) shows the thermal balance for a given part (j–th surface) of the internal furnace walls (as depicted in figure 7). This equation describes the contributions, in a steady operational regime, to the energy equation, where Q_j, which is the heat generated by the electrical resistances, balances the radiation fluxes (coming from other furnace walls, pieces and gases as well as the outgoing flux from the wall) and the convective fluxes (from the gases inside the furnace and exchange through the exterior walls of the furnace)

$$Q_j = \sum_{\substack{j'=1\\ j'\neq j}}^{S_w} \overleftarrow{S_j S_{j'}}\ \sigma T^4_{wall(j')} + \sum_{k=1}^{K} \overleftarrow{S_j \hat{S}_k}\ \sigma T^4_{wp(k)} + \sum_{i=1}^{N} \overleftarrow{S_j G_i}\ \sigma T^4_{cv(i)} -$$
$$-A_j \epsilon_j \sigma T^4_{wall(j)} + \sum_{\substack{control\ volumes\\ in\ contact}} A_{j,i}\ h_j (T_{cv}(i) - T_j) - -A_j h_j{}^{ext}(T_j - T_{room}) \quad (4)$$

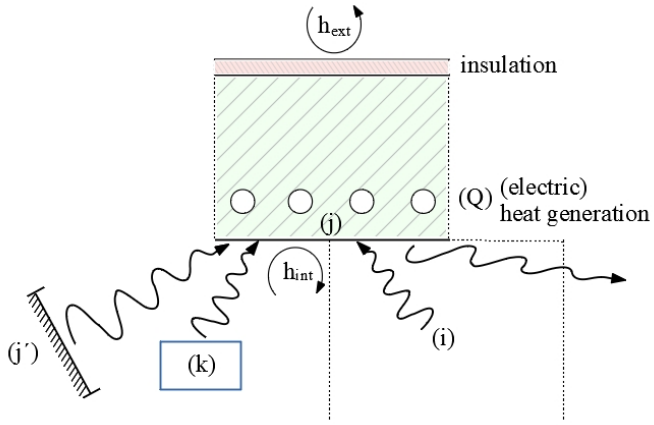

Figure 7: Interaction on a section of the furnace walls

2.2.4 H_2 mass flow balance in a control volume

Over each gas control volume (see figure 8), the mass flow balance of H_2 could be given by equation (5). The injection of H_2 in this control volume, W_i, should be equal to the H_2 mass flow exchanged with the neighboring control volumes and the rates of generation and consumption of H_2 in the reduction/oxidation equation (1).

$$W_i = \sum_{\substack{neighbouring \\ control\ volumes}} \dot{m}_{i,i'}[H_2]_{i'} + \sum_{\substack{working \\ pieces\ in \\ control\ volume}} A_{wp(k)}[k_f(T_{wp(k)}([H_2]_i{}^a - k_b(T_{wp(k)})[H_20]_i{}^b] \quad (5)$$

For the last terms, the kinetics of the forward (reduction) reaction, k_f, and backward (oxidation) reaction, k_b, has been taken into account:

$$r_f = k_f(T)[H_2]^a \quad (6)$$

$$r_b = k_b(T)[H_2O]^b \quad (7)$$

2.2.5 H_2O balance in a control volume

The water vapor mass flow balance in a control volume (as in figure 9) comes from the exchange with neighboring regions, the net rate of generation/consumption from the reduction/oxidation equation and the water vapor freed from the void

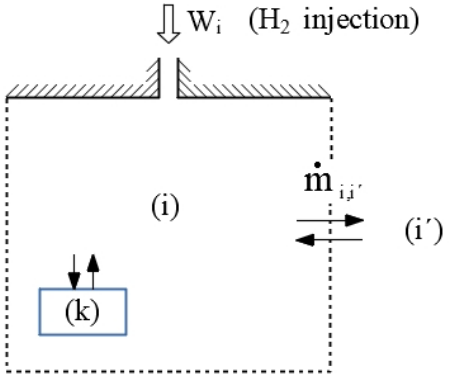

Figure 8: Sketch of a control volume with injection of H_2

inside the pieces, as indicated by equation (8).

$$
\begin{aligned}
0 = & \sum_{\substack{neighbouring \\ control\ volumes}} \dot{m}_{i,i'}[H_2O]_{i'} \\
& + \sum_{\substack{working \\ pieces\ in \\ control\ volume}} A_{wp(k)}[k_d T_{wp(k)}[H_2]_i^{\,a} - k_i T_{wp(k)}[H_2O]_i^{\,b}] + \\
& + \sum_{\substack{working \\ pieces\ in \\ control\ volume}} [\dot{H_2O}]_{wp(k)}
\end{aligned}
\tag{8}
$$

As in the previous section, the kinetics associated to the release of trapped H_2O must be also taken into account:

$$
[\dot{H_2O}]_{wp(k)} = -k_{wr}(T_{wp(k)})[H_2O]^c_{\ wp(k)} \tag{9}
$$

2.3. CFD model of the muffle

As in the zonal models described in the previous sections, similar hypotheses were used to formulate a simplified model for the muffle thermal simulation (see [3] for a similar modeling in a different type of industrial furnace). Except for the obvious transient character of the pieces thermal problem, it is assumed that the furnace operates under steady conditions. Thus, temperature fields for furnace walls in the furnace chamber are both assumed to be steady. At the same time, the gases inside the muffle were considered to be not participating in the thermal radiation. Therefore, thermal radiation is then

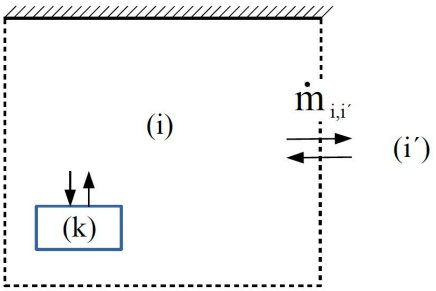

Figure 9: Example of a H_2O mass flow balance for a control volume.

reduced to a surface–to–surface problem restricted to solid surfaces (furnace walls, workpieces surfaces and conveyor belt surface).

The complete model will be decomposed in three submodels concerning, respectively: (a) heat transfer in furnace walls and radiating surfaces, (b) thermo-fluid dynamics of H_2, H_2O and N_2 gases inside the muffle chamber, and (c) heating of the pieces itself. In this section, each of these submodels (as well as its coupling in order to obtain the global CFD model) will be presented.

2.3.1 Thermal model for the furnace walls

According to the previously stated hypotheses, a steady conduction problem must be solved on the furnace walls domain. The furnace walls are formed by some materials with specific (non uniform) thermal conductivity k_s. As this material is object to degradation of its thermal properties between maintenance periods, it seems relevant to include it in the thermal evaluation of the problem. Electric resistances, uniformly distributed inside the furnace, generate a net constant heat source Q when working under steady operational conditions. On the external boundary, cooling by the ambient will be described using a very simple model where heat transfer coefficient h is to be adjusted in order to describe local cooling conditions (and T_∞ stands for the local ambient temperature in the industrial plant). Also, a layer of insulation material is expected to be present near the external surface. In turn, heat exchange through internal walls will be obtained by the composition of a convective heat flux (from the gases inside the furnace) q_{conv} and a (net) radiation heat flux q_{rad}.

$$-\nabla \cdot (k_s \nabla T_s) = Q \tag{10}$$

$$-k_s \frac{\partial T_s}{\partial n} = h(T_s - T_\infty) \qquad \text{on} \quad \Gamma_{ext} \tag{11}$$

$$-k_s \frac{\partial T_s}{\partial n} = q_{conv} + q_{rad} \qquad \text{on} \quad \Gamma_{int} \tag{12}$$

In order to obtain the radiation heat flux on a surface element (assuming that the total radiative surface has been decomposed into N_{rad} elements) we have for the net radiation heat flux (on the k–th surface element)

$$q^k_{rad} = \sigma \epsilon_k \left(T^4_k - \frac{1}{\epsilon_k A_k} \sum_{j=1}^{N_{rad}} G_{jk} A_j \epsilon_j T^4_j \right) \tag{13}$$

as a function of Gebhart factors, G_{jk}, temperatures, T_j, emissivities, ϵ_j, and areas, A_j, of all the radiative surfaces in the enclosure.

The set of radiative surfaces is composed by all the interior walls of the furnace, including the conveyor belt and the workpieces surfaces. In order to compute the radiation heat flux, the workpieces surface temperature will be obtained from the corresponding submodel (see below).

2.3.2 Thermal model for the furnace gases

A second submodel corresponding to the gases domain inside the furnace must be solved to describe heat transfer from gases in the muffled chamber in order to obtain the Reynolds-averaged density, ρ_g, velocity, $\vec{U}$, and temperature, T_g, of the gases. The thermo–hydrodynamical (steady) model for the mixture of gases is described by Reynolds–averaged compressible Navier–Stokes equations and the energy conservation equation (for non–reactive gases), for which the turbulent Reynolds stress tensor τ^R is described by a standard $k - \epsilon$ model as follows

$$\nabla \cdot \left(\rho_g \vec{U} \right) = 0 \tag{14}$$

$$\nabla \cdot \left(\rho_g \vec{U} \otimes \vec{U} \right) + \nabla P - \nabla \cdot \left(\mu_g (\nabla \vec{U} + (\nabla \vec{U})^T \right) = \nabla \cdot \tau^R \tag{15}$$

$$\tau^R = \rho_g \nu_T \left(\nabla \vec{U} + (\nabla \vec{U})^T \right) \quad \text{with} \quad \nu_T = C_\mu \frac{k^2}{\epsilon} \tag{16}$$

$$\nabla \cdot \left(\rho_g c_g \vec{U} T_g \right) - \nabla \cdot \left((k_g + \rho_g c_g \frac{\nu_T}{Pr_t}) \nabla T_g \right) = 0 \tag{17}$$

$$\nabla \cdot \left(\rho_g \vec{U} k \right) - \nabla \cdot \left((\mu_g + \rho_g \frac{\nu_T}{\sigma_k}) \nabla k \right) = \tau^R : \nabla \vec{U} - \rho_g \epsilon \tag{18}$$

$$\nabla \cdot \left(\rho_g \vec{U} \epsilon \right) - \nabla \cdot \left((\mu_g + \frac{\rho_g \nu_T}{\sigma_\epsilon}) \nabla \epsilon \right) = C_{\epsilon 1} \frac{\epsilon}{k} \tau^R : \nabla \vec{U} - C_{\epsilon 2} \rho_g \frac{\epsilon^2}{k} \rho_g \epsilon \tag{19}$$

where Pr_t was chosen equal to 0.9 while the rest of the constants involved in the turbulent model (C_μ, σ_k, σ_ϵ, $C_{\epsilon 1}$ and $C_{\epsilon 2}$) were equal to the standard ones. μ_g, k_g and c_g stand for gases viscosity, thermal conductivity and specific heat, respectively.

The gases mixture will be formed by $N(=3)$ species: N_2, H_2 and H_2O. The latter two are driven by the reduction (forward) or oxidation (backward) reaction (1) that takes place at the piece surface. For inox steels, the metal more prone to form oxides is Cr.

The ideal gas relationship for the mixture (of molecular weight W)

$$P = \frac{\rho_g}{W} R_u T_g \tag{20}$$

should be completed with the mass fraction equations Y_i for each species i, such that:

$$\rho_g = \sum_i^N \rho_i Y_i \tag{21}$$

$$W = \frac{1}{\sum_i^N \frac{Y_i}{W_i}} \tag{22}$$

where only $N-1$ mass fraction transport equations need to be computed (due to $\sum_i^N Y_i = 1$ mass conservation property):

$$\nabla \cdot \left(\rho_g \vec{U} Y_i \right) - \nabla \cdot \left(\rho_g (D_i + \frac{\nu_T}{Sc_t}) \nabla Y_i \right) = 0 \tag{23}$$

being the turbulent Schmidt number Sc_t commonly taken equal to Pr_t.

Equations (17) and (23) represent the energy and mass transport equation for nonreactive species in the gases domain (right-hand terms in the equations equal to 0). However, the numerical model might take into account the production and consumption terms for H_2 and H_2O with the appropriate boundary conditions at the surfaces of the pieces. As an example, the cells in contact with the pieces have a source term for the transport equation of H_2 equal to:

$$S_{H_2} = -\rho_g W_{H_2} \left(k_f(T_g) \left[\frac{\rho_g Y_{H_2}}{W_{H_2}} \right]^y - k_b(T_g) \left[\frac{\rho_g Y_{H_2O}}{W_{H_2O}} \right]^y \right) \tag{24}$$

where k_f and k_b stand for the constants of the forward and backward reaction given by eq. (1).

Standard wall laws can be applied for furnace internal walls and workpieces surfaces boundary conditions where the wall temperature is obtained from the solution of the corresponding submodels. At the mass flow injection inlets, temperature, composition and velocity of the gases mixture are to be imposed. Inlet turbulent parameters should also be specified.

Boundary conditions of temperature, composition, velocity of the gases mixture and/or pressure at the pieces inlet and outlet zones are critical as they account for the global gas flow inside the complete furnace. A good idea seems to combine the information given by the global zone model with the CFD model through the boundary conditions in these sections.

2.3.3 Thermal model for the workpieces

Finally, a model describing heating of steel workpieces in the furnace must be provided. This model will be given by the transient heat equation (25) for the piece temperature field T_p and the suitable boundary conditions for the heat transfer at the pieces walls (26)

$$\rho_p c_p(T_p)\frac{\partial T_p}{\partial t} - \nabla \cdot (k_p(T_p)\nabla T_p) = 0 \tag{25}$$

$$-k_p(T_p)\frac{\partial T_p}{\partial n} = q_{rad} + q_{conv} \tag{26}$$

where q_{rad} and q_{conv} stand for radiation and convective, respectively, heat flow. In order to avoid the difficulties of a moving mesh problem, the pieces are considered to occupy fixed positions inside the computational domain during a given residence time, that is, the total residence time of each piece inside the muffle divided by the number of pieces inside the muffle region. For a given piece position (k), the initial temperature field of the piece will be given by the final temperature field acquired from position ($k-1$) and so on.

In this model, q_{rad} and q_{conv} will be obtained from the previous submodels. A conduction term q_{cond} (corresponding to conduction from the conveyor belt) must be added if the contact surface between pieces and conveyor belt is significant.

2.3.4 Simplified CFD thermal model for the muffle

As an example of the possibilities of the CFD model, a simplified problem was tackled during the modeling week by the team. In particular, submodel in section 2.3.2 for the gases for a unique-component gas was solved for the computational domain of figure 10 with the academic version of software Ansys/Fluent©. Uniform temperatures for the furnace walls and for the conveyor belt respectively were prescribed following the data provided by EcoMT. A prescribed temperature curve for the pieces was also imposed. Specific mass flow rates at the gases injection area were taken from real data of the furnace operation. Concerning the pieces inlet and outlet, different values of the pressure were prescribed to mimic either incoming or outgoing flows through these boundaries. These boundary conditions represent the coupling between the global zonal mode and the muffle CFD model for the proposed

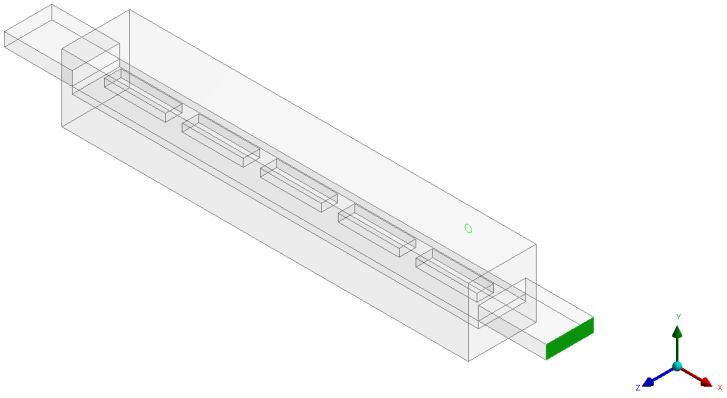

Figure 10: Example of simplified computational domain for the muffle zone.

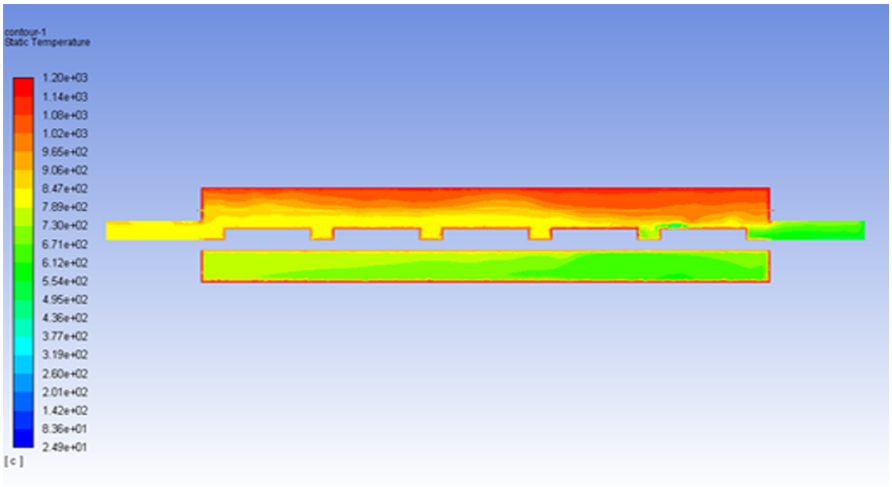

Figure 11: Computational temperature field in the middle plane of the muffle.

approach. Some of the results for the temperature and velocity fields are shown in figures 11 and 12, respectively. The last figure shows the complex velocity patterns that can be found inside the muffle region even for a very simplified model. It is to be remarked (see figure 12 right) that the injected flow is able to provide both a cooling effect of the brazed parts near the injection and a reducing atmosphere in the first part of the muffle.

The results of the complete CFD model, will provide the suitable mass flow distributions to feed, with reliable data, each of the different control volumes considered in the detailed zonal approach.

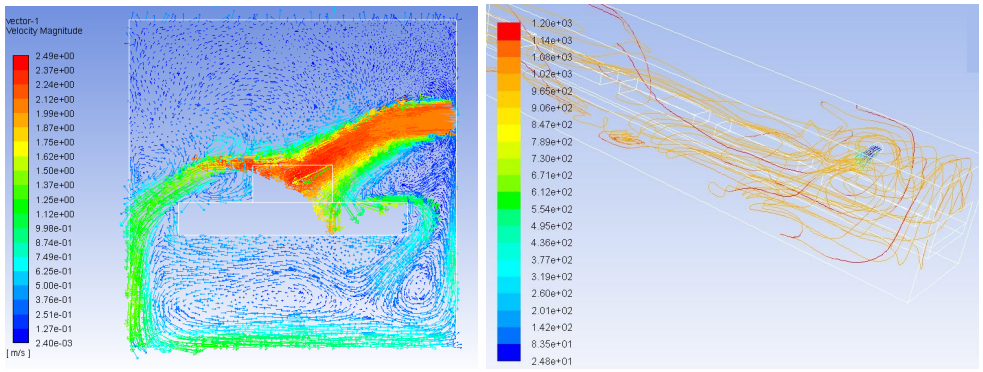

Figure 12: Computational velocity vector field over the piece for a transversal plane located at the H_2 injection area (left). Path lines coming from the H_2 injection (right), colored by temperature.

3. Conclusions

Different models have been presented to mimic the behavior of the complex thermal-fluid dynamic processes involved inside a brazing furnace: a global zone modeling that account for all the six different zones of the process (inlet, pre-heating, reducing, brazing, cooling and exit), a more detailed zone modeling with a decomposition of (at least) the muffle region in different sub-zones (control volumes), and a complex CFD simulation of the muffle region.

These models are complementary, that is, some outputs of the global model are needed as boundary conditions for the CFD of the muffle and, at the same time, some (post-processed) outputs of the CFD model can be used as inputs for the detailed zonal mode.

Some of the parameters involved in the modeling need to be calibrated from measurements from the plant (e.g. parameters of the hydraulic network of the global zone model). Likewise, the whole modeling should be validated through experimental tests (using, for example, DataPaq® measurements for working piece temperatures).

After the necessary validation process, these approaches can lead to a well understanding of the local concentrations of the different gaseous species involved in the problem under different conditions. They can also help to predict the effects generated by the change of a specific operational parameter (e.g. the mass flow injection of H_2, its injection location, conveyor velocity, ...)

However, the models presented are quite far from predicting the brazing process performance in detail, as the problem involves surface tension-driven flows (with dynamic contact lines with variable surface tension due to reactive melting) as well as strong effects of the local thermal pattern on the reactive (due to the allow formation) wetting process, which require much more detailed

models.

References

[1] P. M. Roberts, Introduction to Brazing Technology *Taylor & Fracis Group*, CRC Press 2016.

[2] C. Tan, J. Jenkins, J. Ward, J. Broughton, A. Heeley, Zone modelling of the thermal performances of a large-scale bloom reheating furnace, *Applied Thermal Engineering*, vol. 50, pp. 1111-1118, 2013.

[3] E. Martín, M. Meis, C. Mourenza, D. Rivas, F. Varas, Fast solution of direct and inverse design problems concerning furnace operation conditions in steel industry, *Applied Thermal Engineering*, vol. 47, pp. 41-53, 2012.

Order Reduction on Dynamic Systems using Machine Learning

Academic Coordinator Andrés Gómez Tato
University Galicia Supercomputing Center (CESGA)

Business Coordinator Ángel Rivero Jiménez
Company Repsol Technology Center

Specialist Pablo Solano López
University Technical University of Madrid (UPM)

Team David García-Selfa (University of Santiago de Compostela), Manuel Díaz Méndez (ITMATI), Francisco Pena and Jaime López García (University of Santiago de Compostela and ITMATI), Marco Martinolli (Politecnico of Milano), Bernadett Stadler (Industrial Mathematics Institute, Johannes Kepler University Linz), Naomi Auer (WIAS Berlin), Rocío Calero Fernández-Cortes (UPM), María del Mar González Nogueras (Autonomous University of Madrid) and Umberto Emil Morelli and Francisco Mora Posada (ITMATI)

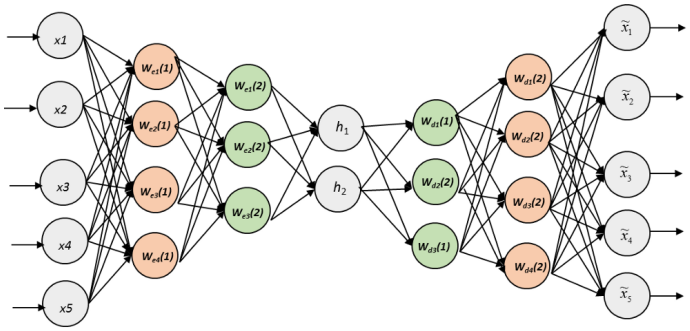

Order Reduction on Dynamic Systems using Machine Learning

Ángel Rivero Jiménez[1], Pablo Solano López[2], Andrés Gómez Tato[3], David García-Selfa[4], Manuel Díaz Méndez[5], Francisco Pena[6], Marco Martinolli[7], Bernadett Stadler[8], Naomi Auer[9], and Umberto Emil Morelli[9]

Abstract

This paper summarizes the results of the P3 group of ESGI 139th event. Due to recent results in the area of Deep Learning for solving Partial Differential Equations, REPSOL proposed to study the possibility of using these techniques in the case of chaotic PDEs as Lorenz or Kuramoto-Sivashinsky equations. Starting from [1] and [2], the workgroup was focused on study these methods and the difficulties to applied to some cases. The main conclusions are that Reservoir networks, as stated by [1], allow to approximate the results of these equations once a initial set of results are produced using other classical methods, but they could be difficult to parameterize and have some issues with the scalability. Also, from [2], the usage of autoencoders could reduce the order of the equations. As consequence, it seems that combining both methods (autoencoder plus Reservoir Neural Networks) could provide a plausible method to make an order reduction on chaotic PDEs which deserves more research.

[1] REPSOL Center of Technology
[2] Área de Ingeniería Aeroespacial, Universidad Rey Juan Carlos
[3] Galicia Supercomputing Centre (CESGA); agomez@cesga.es
[4] Group of Nonlinear Physics, Faculty of Physics, University of Santiago de Compostela (USC)
[5] Technological Institute for Industrial Mathematics (ITMATI) and Politecnico di Milano
[6] Applied Mathematics Department (USC)
[7] Johannes Kepler University Linz
[8] WIAS Berlin
[9] Technological Institute for Industrial Mathematics (ITMATI)

1. Introduction

Solving Partial Differential Equations (PDE) is a complex challenge that frequently has to be done numerically because no other analytical option is available. Depending on which problem to solve, one has to choose the appropriate method and its parameters to achieve a high-quality numerical approximation. This is often translated into expensive computations in terms of memory allocation (fine spatial grids) and computation time (small timesteps), further- more, some applications such as weather prediction, require further tuning in order to force the prediction to follow the real data.

To minimize this kind of risks and to speed up the solutions, there are some techniques that transform the inefficient numerical problem into a smaller one which can be solved faster and produce solutions of similar quality, techniques coined as Model Order Reduction (MOR). One example is the so-called Proper Orthogonal Decomposition (POD)[3].

However, during the last years, Deep Learning [4] has emerged as a powerful tool to solve a large variety of problems from classification of pictures to self-driven cars. The usual workflow is to use a set of real data to create a representation of them that can predict some characteristic of a new future set with high accuracy. So, one possible methodology to control the aforementioned physical problems is to use real data instead of differential equations, i.e., a data-driven solution. The advantage to use Deep Learning, specially Neural Networks (NN), is that they can cope with non-linear problems and, once they are trained, getting a new prediction from a set of data is extremely fast. But it is also possible to follow an alternative method, conceptually similar to MOR techniques: generate an initially set of synthetic data using numerical solutions of PDE and, using Deep Learning, devise a reduced model (from the point of view of computation because is faster by itself or because it uses fewer variables).

Recent publications [1, 2] which addressed the problem of solving chaotic PDEs using Deep Learning techniques spiked the interest of REPSOL about their capabilities to solve real problems. In fact, the Problem 3 of 139th ESGI group tries to answer two initial questions related with the use of Deep Learning for solving PDEs:

- Do we need to keep all the degrees of freedom (dof)? In other words, for a given accuracy, what are the most relevant/optimum modes, that reproduce the dynamics?

- Are numerical methods, and in a further glance, the PDEs, the best way to model, solve and predict the dynamics?

This small paper presents the initial conclusions of the workgroup regarding the usage of these methods for solving PDEs faster. During this week the

authors focused the work in understanding the methods that raised the REPSOL interest and their limitations, centering the advances in two well-known chaotic PDEs with different levels of complexity.

The paper is organized in six sections. The first one is a brief overview of the NN used techniques. For a broader introduction to Deep Learning the reader should look other references as [4]. In this section only relevant information to understand the main results of the workgrop is summarized. Next section explains the importance of PDEs for the industrial sector. It is followed by the main achieved results related to the usage of Reservoir NN following [1]. Section five will analize briefly the usage of autoencoder to finish with the last one which includes the conclusions and recommendations.

2. Neural Networks for a System of Partial Differential Equations

Ever since the development of calculus, Partial Differential Equations (PDEs) have proven to be an incredibly useful tool for physicists and engineers to model the reality both as a variety of continuous and discrete systems. Their utility is that the solutions obtained not only match the physical evolution of studied system but also unravel hidden patterns that might not be measured or detected in a first approach. Unfortunately, in general these PDEs cannot be solved analytically and so they require for approximation techniques that transform the problem into numerical operations a computer can process to get an estimate of the PDE's solution. To obtain such a solution, the usual methods are based on spatio-temporal discretization, i.e., sampling the continous problem into a defined grid. Most common methods found in the literature are finite elements (FEM), finite differences (FDM) or finite volumes (FVM). On one hand, these techniques are very efficient for low-dimensional problems and simple and slightly complex geometries, having proved its performance in many applications in the past decades. On the other, the meshing becomes increasingly difficult for its numerical treatment with the complexity of the geometry. Not only that, the computation goes out of reasonable time scales the moment the problem requires for very high accuracy or spatial resolution. And in addition to all this, most of these algorithms only compute the solution at the grid points and the evaluation of the rest of the domain is then obtained by interpolation or by some other reconstruction technique [5].

As a result of the Cybenko theorem [6], feed forward NN can approximate any continuous function on compact subsets of $\mathbb{R}^n$. Consequently, NN methods can solve both partial and ordinary differential equations. The feed forward NN can then be used as a basic approximation element whose parameter are adjusted during the training to minimize an appropriate error function [7].

The NN provide a differentiable solution with good generalization properties

in close analytic form. This is one of the advantages NN methods have over the aforementioned numerical methods. Moreover, for NN the computational effort does not increase quickly with the number of sampling points. The generality of the method implies that it can be applied to systems independently of their geometrical complexity. Finally, the method can be parallelized and offers an opportunity to solve PDE problems in real time.

2.1. Neural Network Architecture

The number of Neural Networks architectures is constantly increasing and describing all of them is beyond the possibilities of this small summary. In this section only a few of them are described with particular attention to reservoir and autoencoder NN which have been used in the present investigation. Other extensive reviews on the subject are available in the literature [8, 9].

The simplest form of NN is the feed forward NN shown in Figure 1. The direction moves from the input nodes, through the optional hidden nodes and to the output nodes. No cycles or loops are implemented in this architecture. Mathematically, each node i of the hidden and output layer calculates

$$y_i = \mathbf{g}(\mathbf{x^T}\dot{,}\mathbf{w_i} + b_i) \tag{1}$$

where $\mathbf{x}$ is a vector with the inputs comming from the previous layer, $\mathbf{w_i}$ is a vector of unknown parameters (named weights) and b_i is a unknown constant (named as bias), both of them to be fitted, and $\mathbf{g}$ is a bounded non-linear function as *tanh* or *sigmoid*, named activation. When a layer has several nodes,$\mathbf{w_i}$ is transformed in a matrix $\mathbf{W_i}$ where each column is formed by the weights of each node, $\mathbf{b_i}$ is converted in a vector $\mathbf{b_i}$ and the activation function is applied element-wise. This method is applied iteratively layer by layer, resulting on

$$\mathbf{y} = \mathbf{g_i}(\mathbf{g_{i-1}}(\mathbf{g_{i-2}}(...\mathbf{g_1}(x^T \cdot W_1 + \mathbf{b_1})...) \cdot W_{i-1} + \mathbf{b_{i-1}}) \cdot W_i + \mathbf{b_i}) \tag{2}$$

with i is equal to the number of hidden layers plus the output layer. To find the correct values for W_i and b_i, usually a supervised training is executed, where a set of labeled inputs $\mathbf{x_j}, \mathbf{y_j}$ is used to mimimize an objective function which relates the predictions of the NN ($NN(x_j)$) with the labels y_j, frequently applying a gradient descent technique. Because the number of cases is usually very large, the input set is divided randomly in subsets, each one being the input for one optimizacion step. For this reason, the process is known as stochastic gradient descent.

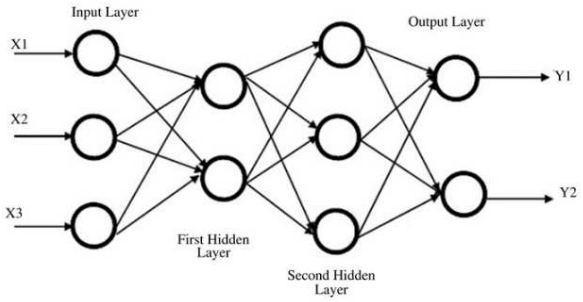

Figure 1: Schematic of a feed forward neural network [7].

Recurrent NN can have connections that go backwards from output nodes to input nodes as well as arbitrary connections between nodes as shown in Figure 2. This kind of networks can preserve sets of data, thus can be said to have a memory. This feature is important when the solution of the problem is dependent from previous inputs.

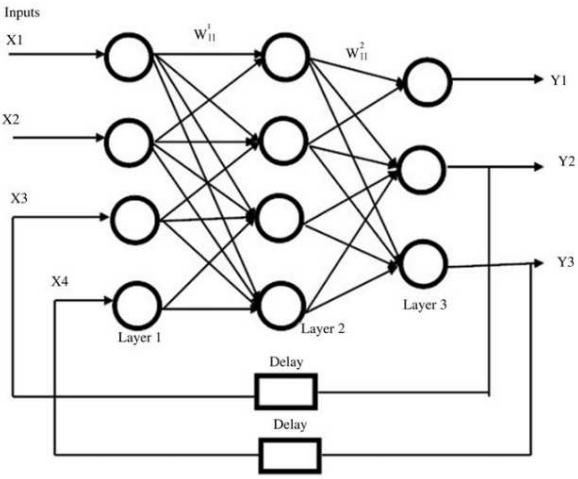

Figure 2: Schematic of a recurrent neural network [7].

One of the neural network used in the present investigation is the reservoir NN. In these networks, an input vector $\mathbf{u}(t)$ of dimension D_{in} is coupled to a high-dimensional dynamical system called "reservoir". As schematically shown in Figure 3, the coupling between the reservoir and the input vector is made by an input-to-reservoir coupler (I/R). From the reservoir, an output vector $\mathbf{v}(t)$ of dimensions D_{out} is coupled through a reservoir-to-output coupler (R/O). The R/O coupler depends on D_r adjustable parameters $\mathbf{p}$. The output $\mathbf{v}(t)$ it creates is assumed to depend linearly to upon the parameters $\mathbf{p}$.

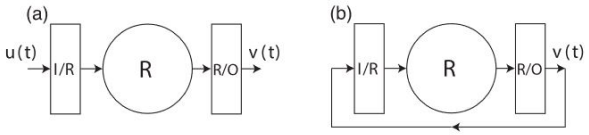

Figure 3: Schematic of a reservoir neural network [1]. (a) Training data gathering phase. (b) Predicting phase.

Being $\mathbf{r}(t)$ the D_r dimensional state vector of the reservoir, it is possible to represent in discrete time ($t = 0, \Delta t, 2\Delta t, \cdots$) the introduced functions as [1]

$$\begin{aligned} \mathbf{r}(t + \Delta t) &= \mathbf{G}\{\mathbf{r}(t), \mathbf{W}_{in}[\mathbf{u}(t)]\} \\ \mathbf{v}(t) &= \mathbf{W}_{out}[\mathbf{r}(t), \mathbf{p}] \end{aligned} \tag{3}$$

where $\mathbf{W}_{in}$ (respectively $\mathbf{W}_{out}$) is a mapping from the D_{in} (D_{out}) dimensional reservoir (output) state space. The system is trained to make $\mathbf{v}(t)$ closely approximate the desired output function $\mathbf{v}_d(t)$ appropriate to the input $\mathbf{u}(t)$.

In the training period $-T \leq t \leq 0$, the training data $\mathbf{u}(t)$ and the resulting $\mathbf{r}(t)$ are used. The output parameters $\mathbf{p}$ are then chosen to minimize the least square difference between $\mathbf{v}_d(t)$ and $\mathbf{v}(t)$ along the training period [1]. Due to the linearity of $\mathbf{v} = \mathbf{W}_{out}[\mathbf{r}, \mathbf{p}]$ with respect to $\mathbf{p}$, $\mathbf{p}$ and $\mathbf{W}_{out}$ are determined through a linear regression [10].

In the present investigation, a reservoir NN is used to predict the evolution of the $\mathbf{u}(t)$. Thus, the network has been trained so that $\mathbf{v}(t)$ is an approximation of $\mathbf{u}(t)$. Consequently after the determination of $\mathbf{p}$, the reservoir system has been to predict the values of $\mathbf{u}(t)$ for $t > 0$.

The response of this NN strongly depends on some parameters that characterize it and that must be accurately selected in the design of a Reservoir NN [11]. The first of this parameter is intuitively the size of the reservoir. Generally, the bigger is the reservoir, the better is the performance of the network. Since the training of the reservoir is cheap compared to other NN, it is common to have size of order 10^4 or bigger [12]. Another parameter is the sparsity of the $\mathbf{W}_{in}$ matrix. This parameter does not have great effect on performance. However, sparsity enables fast reservoir updates when using a sparse matrix representation. [11].

Probably the most important parameter of a reservoir NN is the spectral radius of the reservoir connection matrix $\mathbf{G}$. It scales the width of the distribution of its non zero elements. To ensure echo state properties in practical applications, it is sufficient to ensure that the spectral radius is less than 1. However, in tasks requiring longer memory of the input, the spectral radius should be greater as it affects the influence of previous inputs on the current state. Finally, the input $\mathbf{u}(t)$ can be scaled to keep it bounded and avoid outliers. The input scaling regulates the nonlinearity in the reservoir

representation $\mathbf{r}(t)$ and the effect of the input history. Thus, the input scaling is related to the spectral radius of $\mathbf{G}$.

To conclude this section, a autoencoder NN is described. These are a special case of feed forward NN and are trained to copy the input to the output. It is composed of two parts: an encoder function $\mathbf{h} = F(\mathbf{x})$ and a decoder that produces a reconstruction $\mathbf{r} = G(\mathbf{h})$ [4]. As consequence, $\mathbf{x} - \mathbf{r} \cong 0$.

As feed forward NN, can be trained using minibatch gradient descent following gradients computed by back-propagation but also recirculation can be used [4]. There are different types of autoencoders (sparse, desoising, variational etc.), however they are generally composed of an input layer, set of hidden (encoding) layers reducing the state dimension until the code layer $\mathbf{h}$. Then a set of decoding layers is used to reproduce the input. A schematic of a autoencoder NN is illustrated in Figure 4. For this type of networks, the parameters affecting its performance are the number of layers and the neurons per layer.

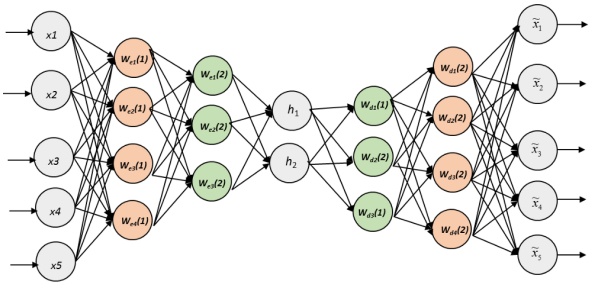

Figure 4: Schematic of a autoencoder NN [13].

3. Challenges for the Industry and the importance of the problem

As we introduced in the previous sections, the rise of the NN techniques. the exponential increase of the know-how and the amount of tools for its development calls for its application into industrial workframes to disrupt classic problems and its solutions. Apart from optimization processes, the recognition of patterns and other machine learning applications more common in the literature, we will focus our attention in the modelling and resolution of physically complex systems.

How so? we will study the implementation of such techniques into the resolution of physical models, written in terms of partial differential equations, with an eye on future learning processes that are only data-driven. This is a twofolded idea: using the efficient NN toolbox as a tool to improve the numerical resolution of PDEs and expanding our modelling capability of

complex systems. We will start and discuss mainly the first aim as it seems a more reachable target for the present work.

Indeed, there is a complicated milestone for the numerical resolution of PDEs: the scalability of the problem. The more spatially and temporary accurate we want our solution to be the bigger and better machines we will need. Not only that, thanks to the better understanding of the subyacent physics, the numerical calculations are now targeting many complex models such as multicomponent flows or visco-elastic materials that increase the expense of the computations even further. One might think that these kind of precissions and studies are only of academic interest, yet the industry is catching up fastly. With the validation of commercial codes, the first order accuracy has become a comodity for simulation and architecture departments of engineering companies and we are walking towards a situation where no more experimental/ test will be required. Indeed, the cutting-edge simulation departments are further and further away from the big number approach.

This pushes into the number of scales the numerical model is required to resolve and the accuracy of that calculation, and unfortunately, even with the lastest algorithms of resolution, the use of parallel supercomputers is still not enough to reach an industrially satisfactory simulation. This issue is often called the high dimensionality problem or even fronteer. The number of dimensions do not necessarily refer to the physical ones but to the number of grid points used for the simulation. In control processes and systems engineering applications might have thousands of such dimensions, or states to be taken into account for the final optimization.

And in those situations the classic finite methodology (differences, elements, volumes, etc.) simply won't work in a feasible a time scale. There have been many attempts in the past regarding this issue, NN is only the last wave of methods that try to deal with this problem. The most recent one are the well-known Monte Carlo techniques, that are nothing but an attempt to apply statistics in a crude manner to reduce the problem. More sofisticated alternatives, with a little more physics inside them are the Modal decomposition, where the solution of the problem is projected into its most fundamental modes or dimensions to then procede with its solution. Although of much more elegancy and even with applications to predict and study the evolution of the problem the mathematic apparatus around them is an important bottleneck, restraining this tools to a more accademic environment.

There is also an important aspect of the scalability problem that made the previous attemps not to reach a fully succesfully agreement: the complexity of the physics that we aim to solve with the numerical model. It was Lorenz one of the first that surprised himself finding out that the system of equations he was using to model the planetary weather was extremely sensible to the initial conditions. Chaos and complexity walk together with the modern models of fluids, making a new challenge appear: we don't only need to solve the

problem, we need to have a temporally accurate solution that includes the correct physics. And classic travel companions such as instabilities and the big elephant in the room, turbulence, makes this point a non-negligible one.

Summing up, the challenge the industry face at this moment is to solve their physical models, that might or not present chaotic and/or unstable behavior, in a very accurate manner in more and more complex geometries and to do this fast and numerically efficient. We believe that NN might help in both reducing the dimensionality of the problem and in the reproduction of the correct physical behavior of the model. Moreover, in a bolder affirmation, in the future even the physical phenomena will be captured or learned by the NN without requiring for a system of PDEs to model it.

4. Reservoir only prediction method

In order to study the applicability of the reservoir only prediction method, we have carried out numerical experiments calculating the usability time or "valid time" for two dynamic systems: **(1)** one of finite dimension, the Lorenz equations, and **(2)** one of infinite dimension, the Kuramoto-Sivashinski (KS) equation. "Valid time" t_v is a quantification of the duration of accurate prediction as defined in [14] with t_v as the elapsed time before the normalized error $E(t_v) < 0.4$.

On the other hand, we have tried to make a calibration of the free parameters of the reservoir looking for that applicability. Used free parameters were:

- β: Tikhonov regularization coefficient
- d: average degree of the random network
- D_r: reservoir size
- ρ: spectral size of the reservoir
- σ: input scaling

4.1. Lorenz equations

The first experiment was made with the Lorenz system, a three-dimensional system that presents chaotic behavior and that is given by the equations,

$$\begin{cases} \dfrac{dx}{dt} = -ax + ay \\ \dfrac{dy}{dt} = bx - y - xz \\ \dfrac{dz}{dt} = -cz + xy \end{cases}, \tag{4}$$

with a=10, b=28 and c=8/3.

For calibration, we have used 20 realizations with different random time intervals for each different parameter sets. And, in order to compare with results obtained in [14], we used the same integration step. The important parameters so far are ρ, σ and D_r [11]. We have taken the values of the parameters whose t_v has been statistically better,

$$\beta = 1.2 \quad , \quad \rho = 0.5 \quad , \quad \sigma = 0.2 \quad , \quad d = 9$$

and we have studied the dependence of t_v with D_r for these values for a training time $T = 20$ Lyapunov times. Training total normalized error is about 0.03. Results are shown in Figure 5.

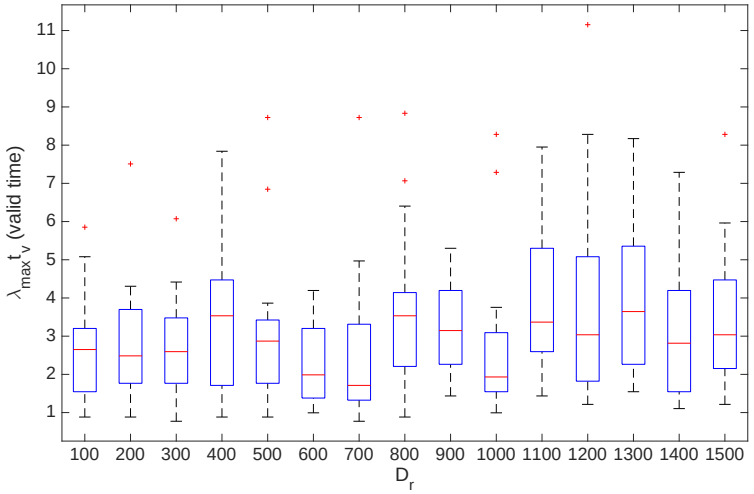

Figure 5: Reservoir size (D_r) dependence of the valid time. The line in the middle is the median value, the top and the bottom of the boxes are the first and the third quartiles, and whiskers delimit 1.5 times the interquartile limits. Crosses mark observations beyond the whiskers.

An example of prediction and the corresponding normalized error are shown in Figure 6, Figure 7 and Figure 8. Predictions starts at $\lambda_{max} t = 0$ and $D_r = 800$.

We can see that the valid time is not very long and covers on average about 2 Lyapunov times. However, dynamics is predicted quite well as we can see in the phase diagram (although rarely loses the dynamics).

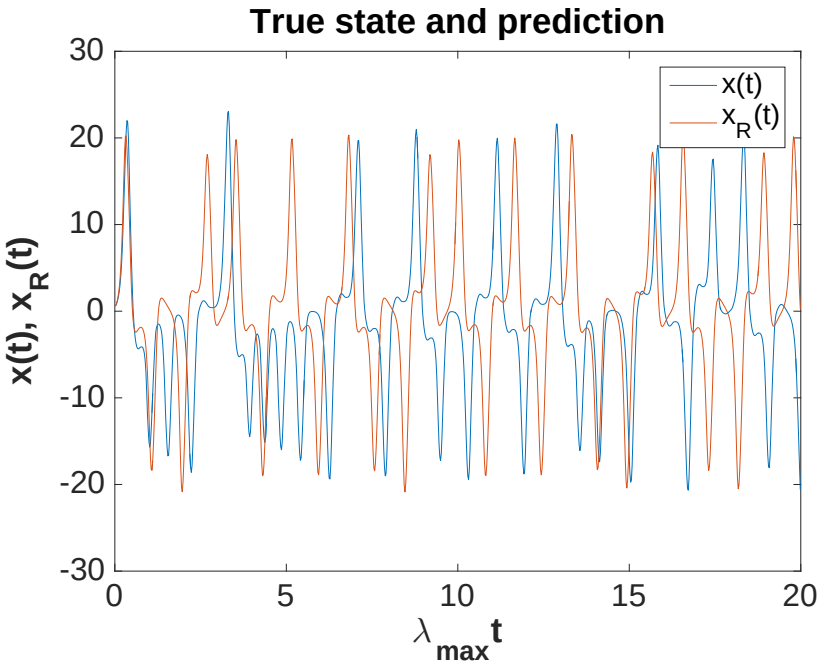

Figure 6: Prediction of the Lorenz system for variable $x(t)$.

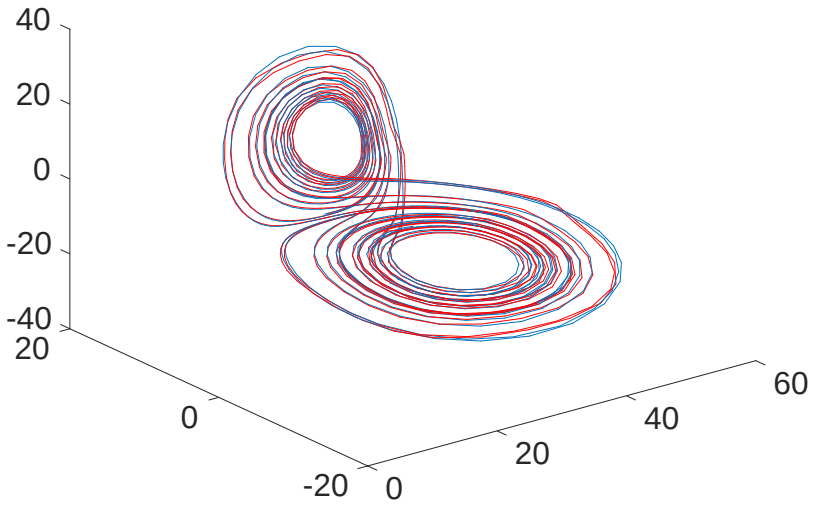

Figure 7: Prediction of the Lorenz system. Phase diagram. Blue line corresponding to exact results and red line corresponding to prediction.

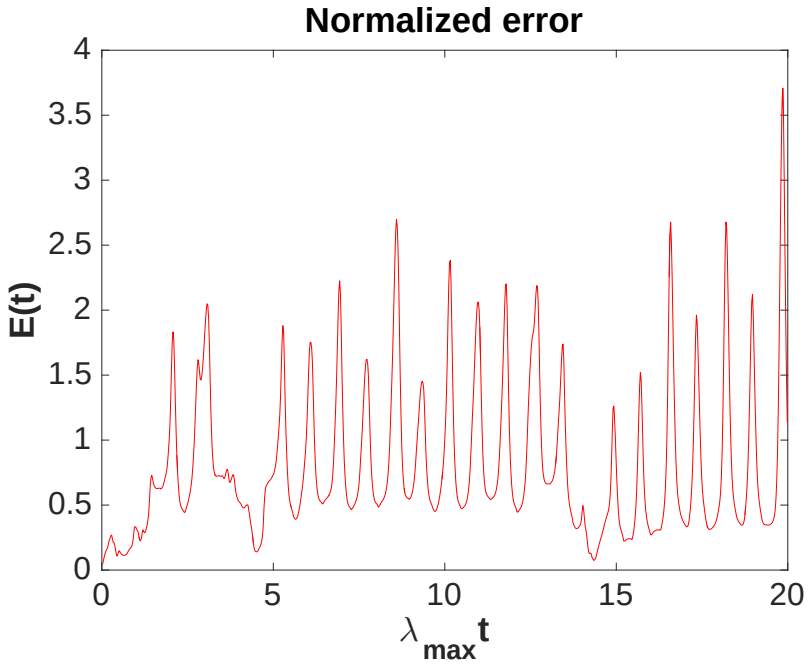

Figure 8: Normalized error for the Lorenz system.

4.2. Kuramoto-Sivashinsky equation

The second experiment was made with the one dimensional Kuramoto-Sivashinsky (KS) equation for $y(x,t)$,

$$y_t = -yy_x - y_{xx} - y_{xxxx} \tag{5}$$

We used the same system size ($L = 34$) with the same spatial discretization ($\Delta x \approx 0.547$) and time sampling ($\Delta t = 0.25$) used in [14].

In this experiment we use 10 realizations in the same time interval. Best values found for reservoir parameters were:

$$\beta = 0.1 \quad , \quad \rho = 0.1 \quad , \quad \sigma = 0.2 \quad , \quad d = 3$$

Training time $T = 14$ Lyapunov times and training total normalized error is about 0.05.

Figure 9 shows (a) σ dependence of the valid time and (b) D_r dependence of the valid time. We found that $\sigma = 0.2$ is the best value. Valid time is better for greater values of D_r, but the larger the reservoir size, the greater the computational cost.

Figure 10 shows a good realization of the experiment for the KS equation, with $t_v = 2.31$ Lyapunov times.

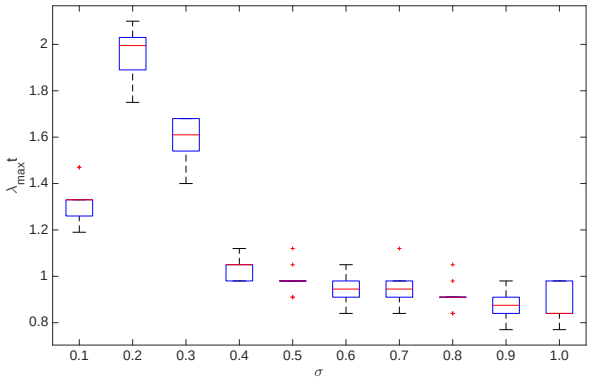

(a) σ dependence

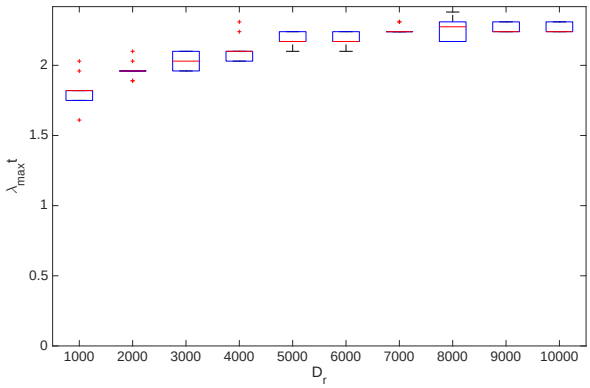

(b) D_r dependence

Figure 9: (a) σ dependence of the valid time with $D_r = 1500$ and (b) D_r dependence of the valid time with $\sigma = 0.2$. Other parameters values: $\beta = 0.1$, $\rho = 0.1$, $d = 3$.

5. Autoencoder

Another possibilitity to reduce the computational effort using NN is to define an autoencoder to reduce the variables where to solve the problem. This is the proposal from [2]. They published the usage an autoencoder which is initialized using a Restricted Boltzmann Machine and in a second step is fine trained as usually with a stochastic gradient descent. Using the encoding part of this autoencoder, they solve a time series reduced problem. Its output can be converted to the original dimensions using the decoding part. Similar approach has been proposed in [15].

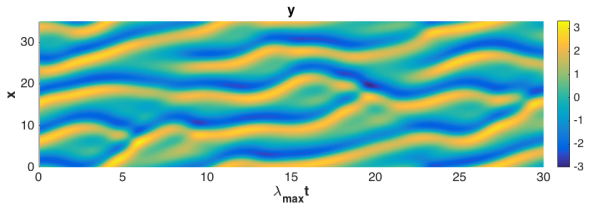

(a) True state

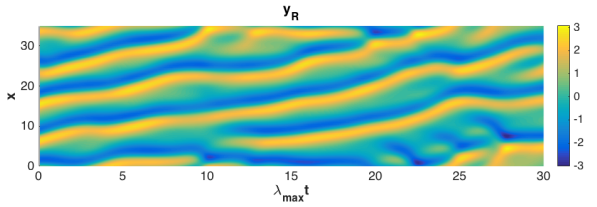

(b) Predicted

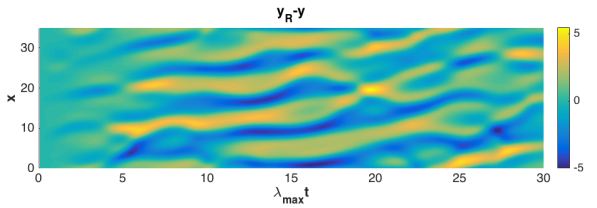

(c) Difference (error)

Figure 10: Parameters values: $\beta = 0.1$, $\rho = 0.1$, $\sigma = 0.2$, $d = 3$, $D_r = 8000$. In this experiment: $t_v = 2.31$ Lyapunov times.

Unfortunately, due to the lack of enough information on the publication, the exact result could not be reproduced. Different autoencoders where tested with several KS results, being extremally difficult to have a valid result, needing a large time to train and they tend to overfit if the caothic regime has to be reproduced accuratelly. Due to this training time, this solution could be valid as a possible technique only if the autoencoder can be trained with a general case and can be used later (maybe with a fast and small retraining) for a problem with different initial conditions on the same domain.

6. Conclusion

Solving PDEs is still a computational challenge. The initial results of this workgroup have shown that Neural Networks could help, reproducing in simple cases the numerical solutions obtained with classical methods for Lorenz and KS equations. However, usage of these computational techniques have also an important work before they can be used in real problems.

Echo State Networks, although currently are not in the mainstream of the

Deep Learning techniques, can alleviate significantly the computational effort for solving the equations for future steps when enough training data have been generated. When this recurrent network has a reasonable number of hidden neurons, its training is very fast, because it needs mainly only two steps: proper initialization and an inverse of one matrix. However, the response of the new trained model depends strongly on some parameters that must be adjusted for each problem[11]:size of the reservoir, sparsity, distribution of nonzero elements, spectral radius, input scaling and leaking rate. These parameters must be calibrated for each problem although the author of [11] assesses that parameters for small cases can be used on bigger ones using transfer learning techniques. Unfortunately, there was no time enough to evaluate this assertion. In any case, the obtained results for Lorenz and KS equations seems that this method can be robust and fast enough to deserve more investigation. Additionally to the necessity of calibrating those hyper-parameters, the main barrier is the scalability of the Reservoir with the size of the problem. Bigger problems will require larger reservoirs. One possible solution is to use several on parallel, using a partition of the domain, as proposed by [1].

On the other size, creating a reduced model using autoencoders is another possible way to reduce the computational cost to solve this set of equations. Following [2], it is possible to reduce the initial spatial domain to a few set of modes or variables which encapsulate the dynamic of the problem, as is done commonly with more classical MOR techniques as POD. The advantage of using Neural Networks based autoencoders is that they can cope with nonlinear functions. In fact, autoencoders have been proposed as a substitute of PCA (related with POD) for this kind of problems. Again, using autoencoders is a computational challenge that need to find the correct values for the hyper-parameters which define the deep network: number of layers, number of neurons for each layer, activations, learning rates, etc. Only if the same configuration and initial weights can be used for any initial conditions of the same problem (or at least, can be transferred with a small fine tuning), the method can really be useful. However, this could not be checked during this week.

If we can assume that there is a general autoencoder for one specific problem independent of its initial conditions and only depending on the geometry and meshing of the domain, there exists the possibility of combining both methods to speed up the solution of PDEs. Initial data is generated solving the equations with traditional methods and after some delay, these data are reduced using the encoding part of the autoencoder, training in this reduced space a Reservoir network which will produce the solution which can be decoded using the second part of the autoencoder. This possibility will be part of the future work.

Additionally to the analyzed cases, during the survey of scientific literature, other methods for solving caothic PDEs have been identified which deserve a future analysis about their usability in the described scenarios. Among them,

[16] proposes to use reinforcement learning techniques. [17] defines a deep learning model based on convolutional and Long Short-Term Memory (LSTM) networks to predict the evolution of physical functions, applying it to fluid flows. The convolutional network reduces the dimensionality of the problem and LSTM are used to make the inference about the temporal evolution of this reduced set of variables.[18] combines a data-driven deep model with a model-driven model to predict the future evolution of a system. [19] follows a different approach to create a neural network from data. He trains a network using a cost function during the training which includes the physical model (i.e., the differential equation), so the NN is forced to approximate the data and to verify the differential equation simultaneously.

In summary, currently the authors cannot answer definitively any of the proposed questions. However, from the results of the executed experiments, the combination of both techniques seems to be a method to be explored deeply because can represent an alternative to current MOR techniques.

References

[1] J. Pathak, B. Hunt, M. Girvan, Z. Lu, and E. Ott, "Model-free prediction of large spatiotemporally chaotic systems from data: A reservoir computing approach," *Phys. Rev. Lett.*, vol. 120, p. 024102, Jan 2018.

[2] M. Wang, H.-X. Li, X. Chen, and Y. Chen, "Deep Learning-Based Model Reduction for Distributed Parameter Systems," *IEEE TRANSACTIONS ON SYSTEMS, MAN, AND CYBERNETICS: SYSTEMS*, vol. 46, no. 12, 2016.

[3] G. Berkooz, P. Holmes, and J. L. Lumley, "The proper orthogonal decomposition in the analysis of turbulent flows," *Annual review of fluid mechanics*, vol. 25, no. 1, pp. 539–575, 1993.

[4] I. Goodfellow, Y. Bengio, and A. Courville, *Deep Learning*. MIT Press, 2016.

[5] J. Berg and K. Nyström, "A unified deep artificial neural network approach to partial differential equations in complex geometries," *ArXiv e-prints*, Nov. 2017.

[6] G. Cybenko, "Approximation by superpositions of a sigmoidal function," *Mathematics of Control, Signals and Systems*, vol. 2, pp. 303–314, Dec 1989.

[7] N. Yadav, A. Yadav, and M. Kumar, *An introduction to neural network methods for differential equations*. Springer, 2015.

[8] M. Egmont-Petersen, D. de Ridder, and H. Handels, "Image processing with neural networks—a review," *Pattern recognition*, vol. 35, no. 10, pp. 2279–2301, 2002.

[9] W. Cao, X. Wang, Z. Ming, and J. Gao, "A review on neural networks with random weights," *Neurocomputing*, vol. 275, pp. 278 – 287, 2018.

[10] X. Yan and X. G. Su, *Linear Regression Analysis*. WORLD SCIENTIFIC, 2009.

[11] M. Lukoševičius, "A Practical Guide to Applying Echo State Networks," in *G. Montavon, G. B. Orr, and K.-R. Müller (eds.) Neural Networks: Tricks of the Trade, 2nd ed. Springer LNCS 7700, 659-686*, 2012.

[12] F. Triefenbach, A. Jalalvand, B. Schrauwen, and J. pierre Martens, "Phoneme recognition with large hierarchical reservoirs," in *Advances in Neural Information Processing Systems 23* (J. D. Lafferty, C. K. I. Williams, J. Shawe-Taylor, R. S. Zemel, and A. Culotta, eds.), pp. 2307–2315, Curran Associates, Inc., 2010.

[13] "Deep autoencoders for collaborative filtering."

[14] J. Pathak, A. Wikner, R. Fussell, S. Chandra, B. Hunt, M. Girvan, and E. Ott, "Hyryd forecating of chaotic processes: Using machine learning in conjunction with knowledge-based model," *ArXiv e-prints*, Mar 2018.

[15] C. Qi and H.-X. Li, "Nonlinear dimension reduction based neural modeling for distributed parameter processes," *Chemical Engineering Science*, vol. 64, pp. 4164–4170, 2009.

[16] S. Wei, X. Jin, and H. Li, "General solutions for nonlinear differential equations: a deep reinforcement learning approach,"

[17] S. Wiewel, M. Becher, and N. Thuerey, "Latent-space Physics: Towards Learning the Temporal Evolution of Fluid Flow," feb 2018.

[18] Y. Long, X. She, and S. Mukhopadhyay, "HybridNet: Integrating Model-based and Data-driven Learning to Predict Evolution of Dynamical Systems," jun 2018.

[19] M. Raissi, P. Perdikaris, and G. E. Karniadakis, "Physics Informed Deep Learning (Part I): Data-driven Solutions of Nonlinear Partial Differential Equations," nov 2017.

Predictive maintenance in a pellet production factory

Academic Coordinator Manuel Febrero Bande
University University of Santiago de Compostela (USC)

Business Coordinator Laura Vázquez Pardo
Company Grupo Gestán

Team María Vázquez García (Grupo Gestán-Biomasa Forestal)

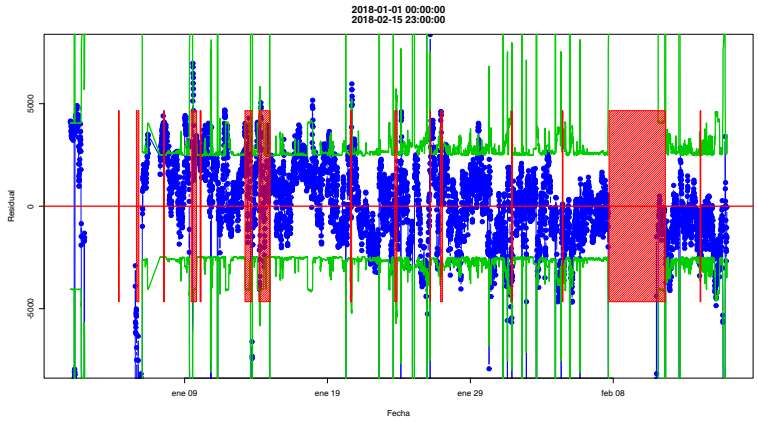

Predictive maintenance in a pellet production factory

Manuel Febrero–Bande[1]

Abstract

The goal of this problem is to analyze the data generated in continuous mode from the factory to find patterns with the aim to anticipate (if possible) future breaks or malfunctions of certain components of the facility. This is called a "predictive maintenance problem". In this case, we must analyze the variables derived from the production process of pellets related with the main components: the dryer, the boiler, the furnace and the packaging system.

1. Presentation of the problem

In this work we study a prediction maintenance problem associated with a facility devoted to the production of pellets. As usual in the Industry 4.0 framework, the production process is fully automated with a lot of sensors along the production line mainly with the goal of controlling the quality of the final product (via controlling the production process). Typically, the process/device/system that must be maintained is composed by several parts or components that are monitored in continuous time. This produces a lot of data from many variables related with the components that is stored with the goal of identifying those situations that can lead the process out of control or when the crash or malfunction of any of the components can be anticipated. In Figure 1 a diagram of the final stage of the production pellet process is shown where the small boxes with numbers inside are related with variables/measures that can be extracted from some components. The small boxes in yellow represent those variables established by managers as desired values that must

Figure 1: Flow diagram of the production line (final stage)

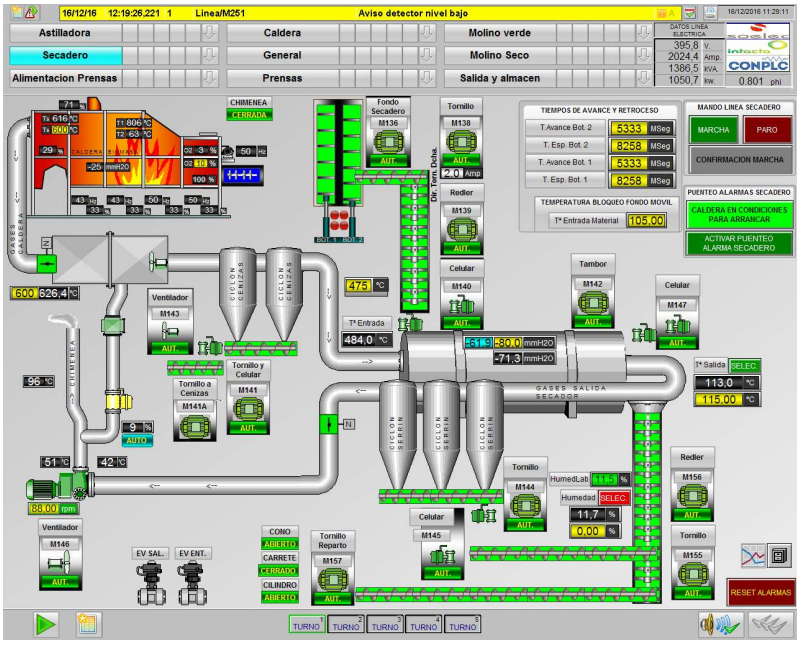

be compared with those obtained by sensors for the control of the process. The names of those variable typically begins with `SP.`

Unfortunately, the situation in this factory respect to the design of the sensors is quite common to other facilities. The sensors are installed with the goal of helping the production process but with no clear idea about how to assess the maintenance problem. For instance, there are few possibilities of cross-checking among the variables because rarely duplicated sensors are installed in the system and sometimes, when a sensor begins to degenerate it is not detected

Particularly, in this case, the quality of the process is measured using the variable `TiempAvance` which is the gap between consecutive feeds of the dryer. Lower values mean that the production process is faster and so all the components and sub-processes are working nearly at its optimal rate. This variate is measured in milliseconds and takes values in the interval [2000,8000].

Related with the response, we have the following variables:
From the dryer: `VelTornM138`, `VelTornM146`, `SP.HumedSec`, `HumedadSec`, `HumedLabor`, `HumedadAstilla`, `PosCompReg`, `SP.DeprSec`, `DeprSecad`
From the boiler: `SP.TmpSalCald`, `TempSalCald`, `TempEntrSec`, `TmpSalSecad`, `TempHogar`, `TempSalHogar`, `O2Caldera`, `AlimCaldera`, `DemSecadero`, `DeprCaldera`, `TempChimen`, `CompCamaraCald`
From the press: `VelTornilloP1`, `ConsumP1`, `ConsumAguaP1`, `HumedadPellestP1`, `VelTornilloP2`, `ConsumP2`, `ConsumAguaP2`, `HumedadPellestP2`

Many of the precedent variables are close related each other and so, if we are planning to construct a regression model with all of these variates, we must pay attention to non include redundant information to avoid numerical instabilities.

2. Exploratory analysis

The first step is every statistical study is always an exploratory data analysis. This step has two goals: find those covariates more related with the response and find clues about the relationship among covariates and even identify those situations with absurd or strange values but included in the database by the continuous monitoring process. In general, the last problem could be avoided if a quality data process were done also continuously over the database.

The first idea for a maintenance problem is to characterize the situation that the process is under control and use that characterization as an advanced indicator that any of the components or the whole process must be maintained/ repaired. In essence, every new datum far from the control zone must be considered suspicious and further investigated. So, the main idea is to predict

[1] Universidade de Santiago de Compostela and ITMATI; manuel.febrero@usc.es

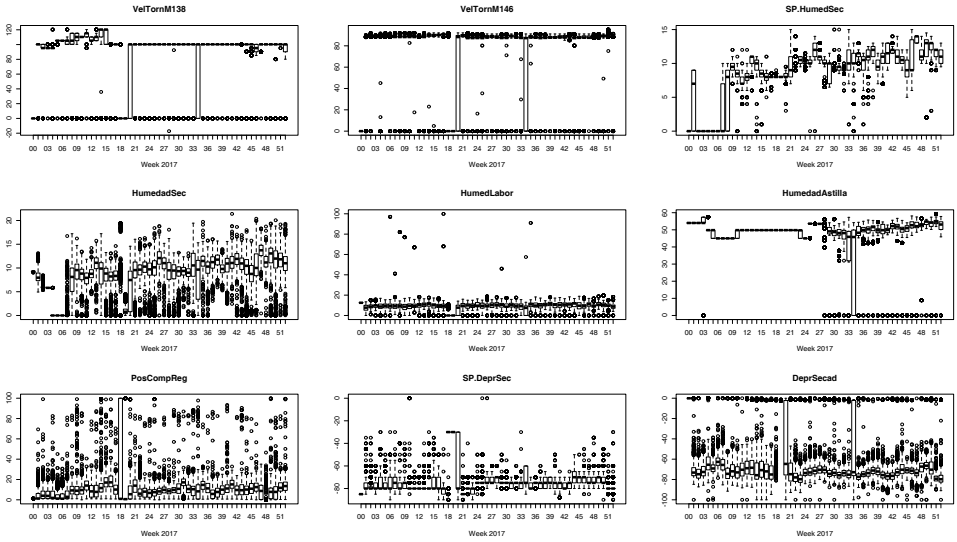

Figure 2: Boxplots of several variables from dryer by week (2017)

also continuously the response with the values measured from the process using filtered information of the historical database of the process (create a filter that ensures that the process is under control) and if the prediction or any other diagnostics of the model deviates significantly from its expectation, label the situation of the process as suspicious.

From the simple boxplots of all covariates that are shown in Figures 2–5 and the deep knowledge about the process, some combinations of values are not possible for an optimal process and so, the first decision is to establish some rules to remove anomalous data from the data avoiding this type of data become part of the final model. For instance, those data where $\texttt{VelTornM138} = 0$ are indications that the production process was stopped. Also, some variables related with temperatures must have certain intervals to be considered valid for a process that it is working smoothly.

The conditions that must fulfill the data to be consider "good enough" are as follows:

1. $\texttt{VelTornM138} > 95$
2. $\texttt{VelTornM146} > 87$
3. $550 < \texttt{TempHogar} < 880$
4. $\|\texttt{SP.DeprSec} - \texttt{DeprSecad}\| < 20$
5. $\texttt{DeprSecad} < -60$
6. $\|\texttt{SP.TmpSalCald} - \texttt{TempSalCald}\| < 20$

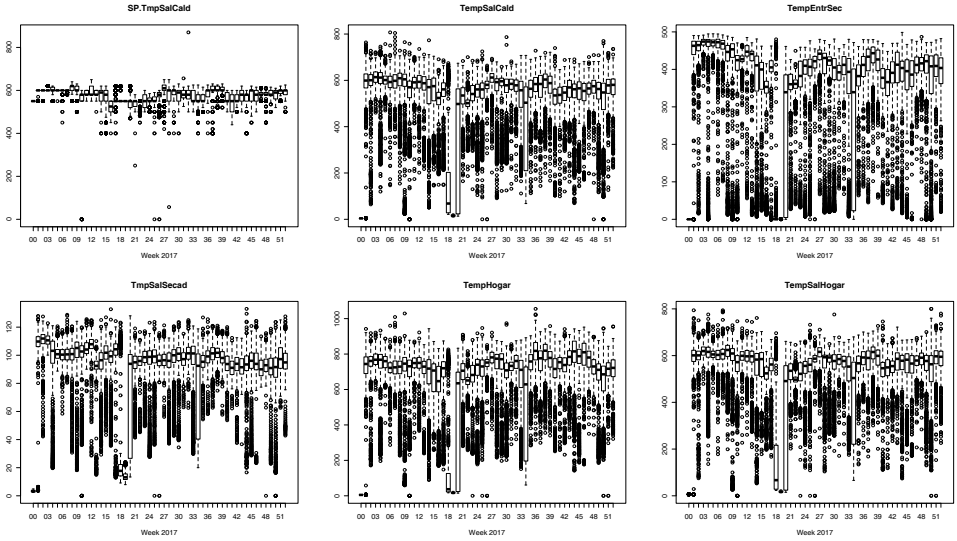

Figure 3: Boxplots of several variables from boiler by week (2017) (I)

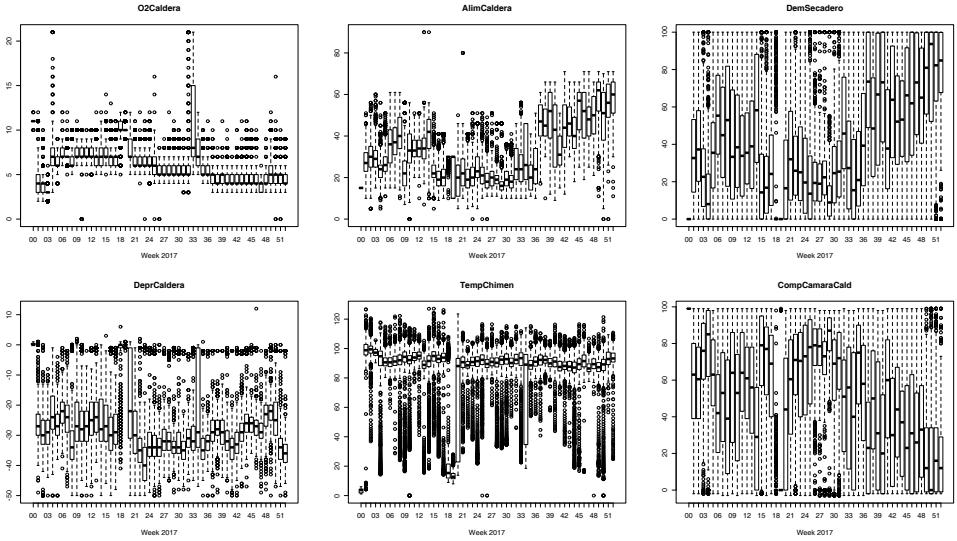

Figure 4: Boxplots of several variables from boiler by week (2017) (II)

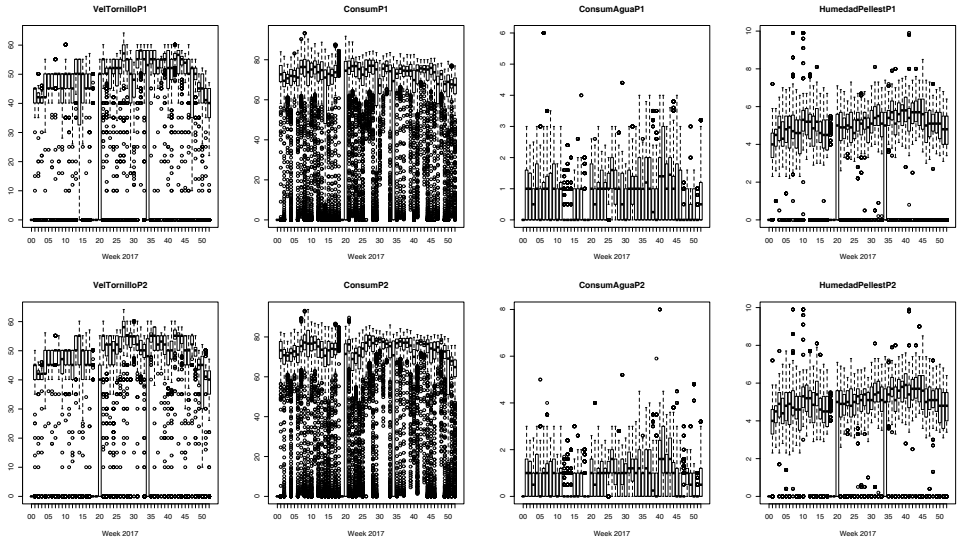

Figure 5: Boxplots of several variables from press by week (2017) (I)

7. $\|\texttt{SP.HumedSec} - \texttt{HumedadSec}\| < 8$
8. $\texttt{HumedadSec} \geq 5$
9. $\texttt{PosCompReg} < 20$
10. $\texttt{SP.HumedSec} > 7$
11. $\texttt{HumedadAstilla} > 40$
12. $\texttt{TempEntrSec} > 300$
13. $\texttt{TempChimen} < 110$
14. $\texttt{DeprCaldera} < -15$
15. $\texttt{VelTornilloP1} + \texttt{VelTornilloP2} > 80$

The previous filters are using the 38.3% of the original data. Although this can be considered excessively high, the aim is to find a dataset where we must be confident that the production process is working fine.

Now the boxplots of the filtered data are shown in Figures 6–9, which will be the data used for constructing the regression model.

3. Modelling

The next stage is to select from the whole set of variables, an optimal subset that can be able to predict accurately `TiempAvance`. For this purpose, we

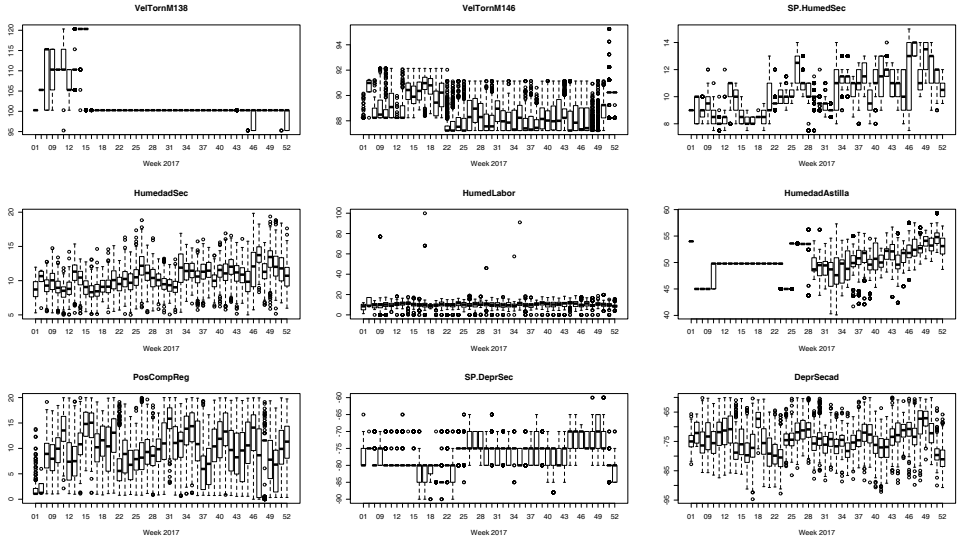

Figure 6: Boxplots of several filtered variables from dryer by week (2017)

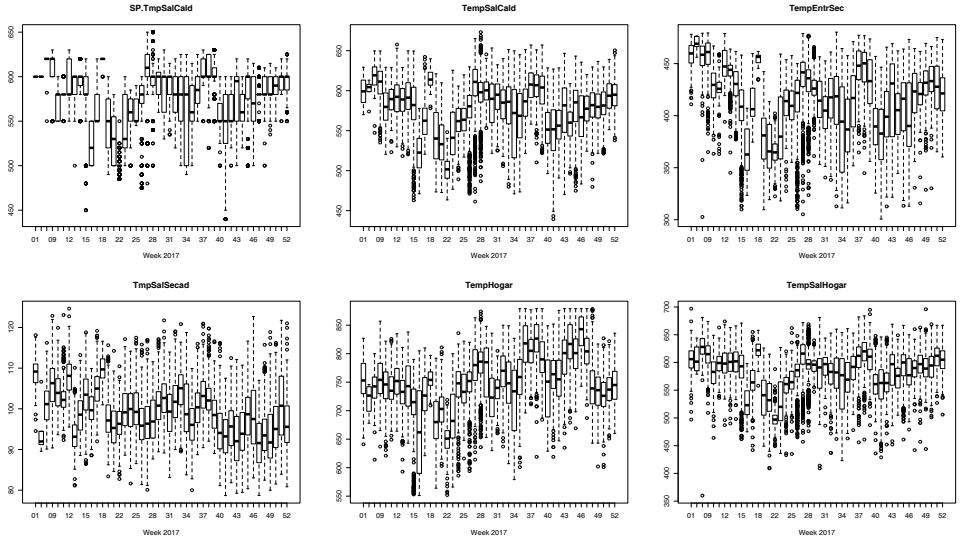

Figure 7: Boxplots of several filtered variables from boiler by week (2017) (I)

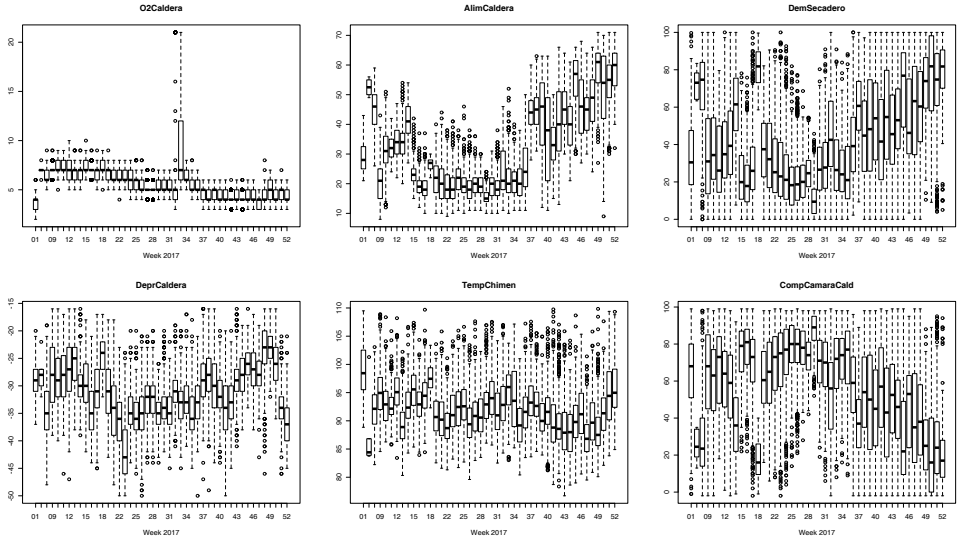

Figure 8: Boxplots of several filtered variables from boiler by week (2017) (II)

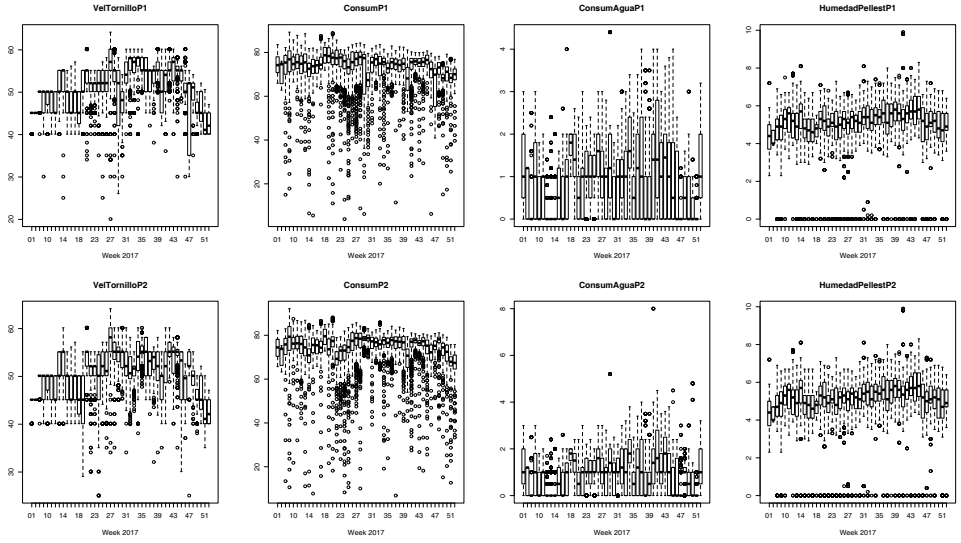

Figure 9: Boxplots of several filtered variables from press by week (2017) (I)

will employ the Distance Correlation, $\mathcal{R}$, (see [2] and [1]) which is a recent development that has better properties than the classical Pearson correlation coefficient. In particular, the $\mathcal{R}$ characterizes independence among variables of arbitrary dimensions whereas the Pearson only characterizes independence among univariate gaussian variables. This means that the Distance Correlation can detect complexer relationships among variables than the linear.

In the following table, the Distance Correlation with `TiempAvance` is shown for every covariate.

```
>    VelTornM138    VelTornM146    SP.HumedSec     HumedadSec     HumedLabor
>          0.095          0.761          0.089          0.064          0.099
> HumedadAstilla     PosCompReg     SP.DeprSec      DeprSecad
>          0.098          0.267          0.097          0.137
>  SP.TmpSalCald    TempSalCald    TempEntrSec    TmpSalSecad       TempHogar
>          0.072          0.051          0.144          0.293          0.072
>   TempSalHogar      O2Caldera    AlimCaldera    DemSecadero    DeprCaldera
>          0.053          0.076          0.144          0.097          0.124
>     TempChimen CompCamaraCald
>          0.167          0.096
>    VelTornilloP1         ConsumP1     ConsumAguaP1 HumedadPellestP1
>            0.135            0.159            0.200            0.057
>    VelTornilloP2         ConsumP2     ConsumAguaP2 HumedadPellestP2
>            0.129            0.178            0.202            0.062
```

The interpretation of $\mathcal{R}$ is similar to the determination coefficient. All values of $\mathcal{R}$ are in the interval $[0, 1]$ and the relevant variables for explaining the response must be selected from the subset of higher values of these vectors.

The modeling task is a forward/backward procedure that at each step must evaluate all the candidates variables (those not in the model) to select which one could become part of the model and with what type of contribution (linear, smooth, ...). If we restrict ourselves to use only linear contributions, the problem of constructing an optimal model is quite well solved in literature but this is not true for smooth contributions. In this latter case, the task must be done manually and sequentially, analysing with care the diagnostics of the model at every step. As a general rule, the best candidate to become part of the model is that variable that stores more information not included in the variables already in the model. This can be done computing distance correlation among the residuals of the model and the new candidates to enter in.

```
....

> Parametric coefficients:
>              Estimate Std. Error t value Pr(>|t|)
> (Intercept) 77857.083    440.737   176.7   <2e-16 ***
> VelTornM146  -826.389      4.976  -166.1   <2e-16 ***
> ---
> Signif. codes:  0 '***' 0.001 '**' 0.01 '*' 0.05 '.' 0.1 ' ' 1
>
> Approximate significance of smooth terms:
>                                edf Ref.df      F p-value
> s(I(SP.HumedSec - HumedadSec))  6.527  7.597 109.36  <2e-16 ***
```

```
> s(HumedadAstilla)                8.929  8.998  64.08  <2e-16 ***
> s(TmpSalSecad,TempEntrSec)      28.219 28.959  52.38  <2e-16 ***
> s(DeprSecad)                     7.624  8.476  13.30  <2e-16 ***
> s(AlimCaldera)                   8.545  8.934 164.93  <2e-16 ***
> s(DeprCaldera)                   5.113  6.221  23.56  <2e-16 ***
> s(TempChimen)                    6.309  7.385  35.00  <2e-16 ***
> s(VelTornilloP1,VelTornilloP2) 26.546 28.592  73.76  <2e-16 ***
> R-sq.(adj) =  0.713   Deviance explained = 71.5%
> GCV = 6.0592e+05  Scale est. = 6.0292e+05  n = 20101
```

After a careful application, the list of the variables in the final model can be seen in the previous summary. Twelve variables were selected with only one with a linear contribution (`VelTornM146`) that was also the variable with the highest distance correlation with the response. The rest of the variables enter with a smooth contribution with certain differences among them:

1. The variables related with the humidity of the dryer enter as a function of the difference: `SP.HumedSec-HumedadSec`

2. The variables related with temperatures of the dryer enter as a function of two arguments:`TmpSalSecad, TempEntrSec`.

3. The variables related with the press enter the model also as a function of two arguments: `VelTornilloP1, VelTornilloP2`.

Also from the summary we can order the smooth variables by its importance looking at the column F. Higher the value, greater the importance. This can be also seen in the partial effects in Figures 10 and 11 checking the scale of the functions. The interpretation of these figures are quite easy. Those intervals where the function is over 0 lead to worse performance. And, on the contrary, negative values of the function lead to better performance of the process. In the bivariate functions, the best combinations are obtained in the red zones.

4. Checking with data from 2018

The final analysis is to check how the model works in a range of dates not included in the model to assess what would be its performance in practice. Also, the incidents recorded by the facility were incorporated to check how the model on that cases. In the following figures (Figures 12–14) the residuals of the model (as blue points) are shown respect to its confidence interval at 95% (green line). The incidents are plotted in red with rectangles that covers the whole incident. So, every time that a blue point is out the interval it may be considered that the process is out of control. Also, those times that the interval have peaks mean that the process is providing values that are not in the core of what was selected for the model and must be considered suspicious. Finally, we must also pay attention to runs (increasing or decreasing patterns) in the blue points even though these runs were inside the intervals provided.

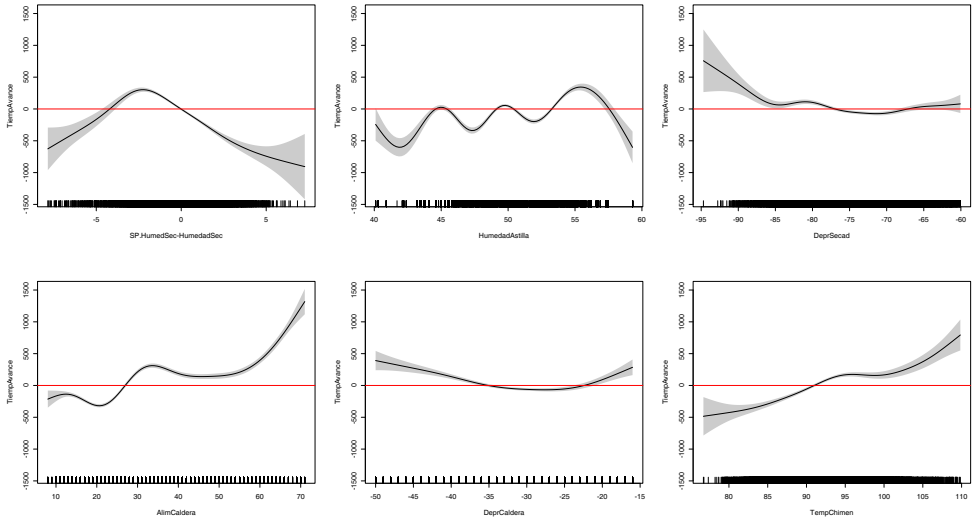

Figure 10: Partial effects for the univariate smooth functions

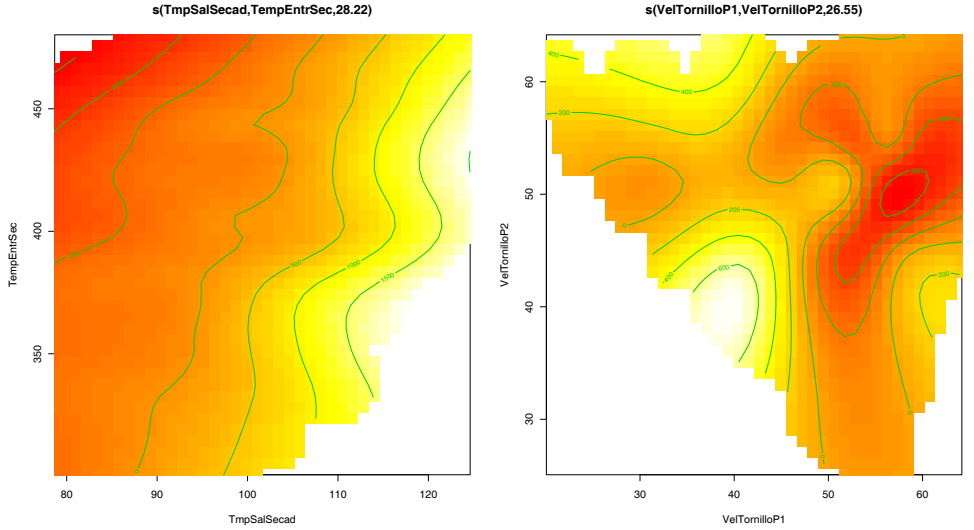

Figure 11: Partial effects for the bivariate smooth functions

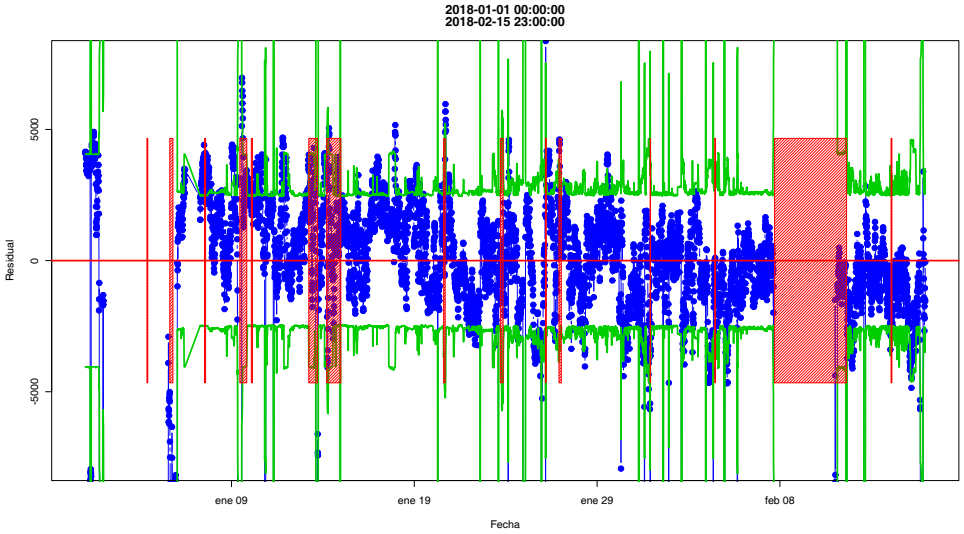

Figure 12: Prediction for period: 01/01/2018–02/15/2018

The period between 01/01/2018 and 02/15/2018 was quite unstable in terms of incidents and this is quiet well reflected in the previous figure. The next period (02/16/2018–03/31/2018) is more stable with a clear run (decreasing and then increasing) between 03/15/2018 and 03/25/2018 that must be carefully analysed.

A good example of the process under control is the last figure (Figure 14). After a chaotic path and a maintenance task made in the first three days of May, the residuals and the intervals are quite tight and completely under control for the rest of the days.

5. Conclusions

This is a concept test about a pathway that may end in an effective predictive maintenance procedure. The preliminary results seem quite promising but more work is needed on selecting information and on developing other models for the intermediate variables. The final stage would be a hierarchical model where all the variables in the dataset can be modelled and controlled. With that kind of model, when the process is going out of control, it would be possible to check what is the source of instability.

More work is needed in the analysis of the signals to discard anomalous measurements with the goal of constructing a clean reference dataset. Probably, some new sensors must be added to cross-check the values provided. These new sensors must act as backups to detect when a sensor degenerates. Alternatively, the quality of the information provided by the installed sensors may be assessed

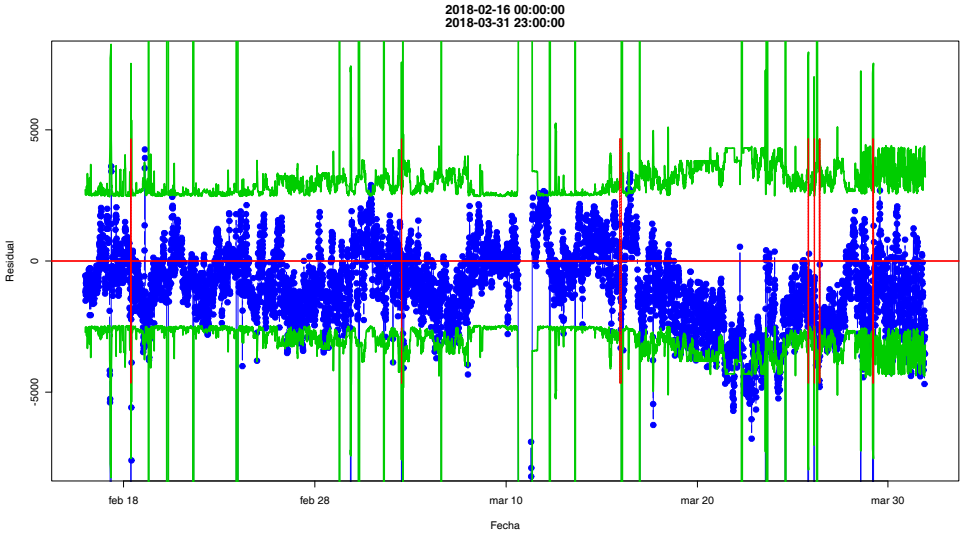

Figure 13: Prediction for period: 02/16/2018–03/31/2018

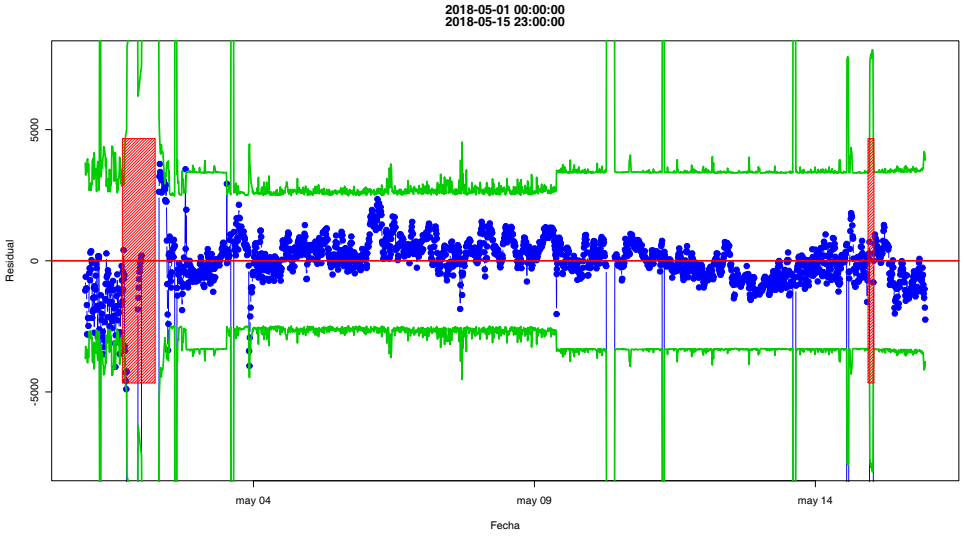

Figure 14: Prediction for period: 05/01/2018–05/15/2018

through implementing calibration protocols of the measures.

References

[1] Gábor J Székely and Maria L Rizzo. The distance correlation of independence in high dimension. *J Multivariate Anal,* 117:193-213, 2013.

[2] Gábor J Székely, Maria L Rizzo and Nail Bakirov. Measuring and testing dependence by correlation of distance. *Ann Stat,* 35(6):2769-2794, 2007.

Equivalent thermo-mechanical model for ceramic cups

Academic Coordinators Peregrina Quintela Estévez and Patricia Barral Rodiño
University Universidade de Santiago de Compostela (USC) and Technological Institute for Industrial Mathematics (ITMATI)

Business Coordinator Miguel Fanjul Cuesta
Company ArcelorMittal

Specialist María Teresa Sánchez Rúa
University Centro Universitario de la Defensa (Zaragoza)

Team Javier Bullón, Luis Javier Pérez Pérez, Iván Martínez Suárez and Sara Vázquez Fernández (USC) and Nirav Vasant Shah (Scuola Internazionale Superiore di Studi Avanzati (SISSA), Trieste, Italy)

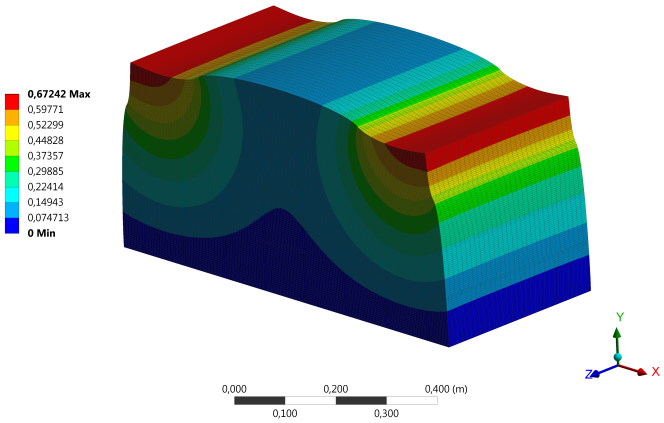

Equivalent thermo-mechanical model for ceramic cups

P. Barral[1], M. Fanjul[2], L.J. Pérez-Pérez[3], P. Quintela[4] and M.T. Sánchez[5]

Abstract

The ceramic cup of a Blast Furnace (BF) is an assembly of refractory bricks and joints composed of castable refractories. Due to its location inside the wall of a Blast Furnace, it has to sustain harsh operation conditions. In particular, temperatures reach 1500°C. Thus, big thermal stresses and strains are expected. In order to perform numerical simulations that accurately assess the thermo-mechanical behaviour of the ceramic cup, both the castable joint and the refractory brick would need to be considered as different materials. However, the ceramic cup is constructed with many bricks, which are also very different in size when compared to the joints. This leads to computational costs that are unfeasible, since each individual brick and joint have to be considered in the mesh of the domain.

Consequently, the challenge proposed by the steelmaking company ArcelorMittal for the 139 ESGI was to find an equivalent thermo-mechanical model that enables to circumvent this difficulty. In this work, we assume that the assembly of bricks and joints may be homogenized as an anisotropic linear elastic material. In order to find the relevant parameters of the homogenized material, we follow a methodology that performs different mechanical tests in a unit cell considering the two different

[1] Universidade de Santiago de Compostela and Instituto Tecnológico de Matemática Industrial; patricia.barral@usc.es

[2] ArcelorMittal I+D, Avilés, Spain

[3] Universidade de Santiago de Compostela; luisjavier.perez@usc.es

[4] Universidade de Santiago de Compostela and Instituto Tecnológico de Matemática Industrial; peregrina.quintela@usc.es; peregrina.quintela@itmati.es

[5] Centro Universitario de la Defensa, Academia General Militar, Zaragoza; tererua@unizar.es

materials. Finally, the response of the homogenized anisotropic material is compared to the response of the two different materials in an assembly of several unit cells.

1. Introduction

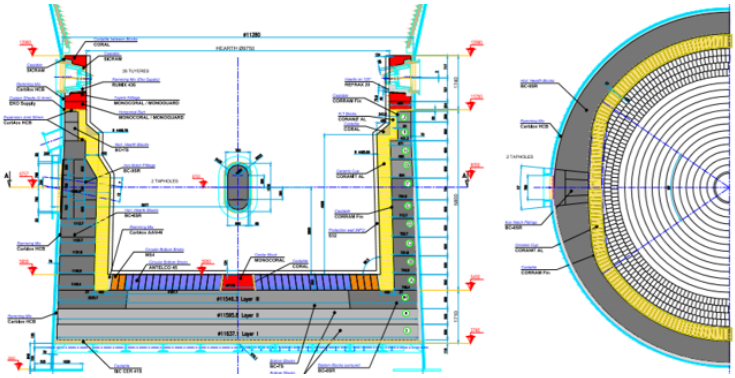

Figure 1: Blast furnace hearth drawings with the ceramic cup highlighted in yellow. Source: ArcelorMittal.

ArcelorMittal is the world's largest steel producer, formed in 2006 after the merger of the steel maker Arcelor (Spain, France and Luxembourg) and the indian company Mittal Steel. It has around 200,000 employees in more than 60 countries and is involved in both mining and steelmaking activities. ArcelorMittal is also at the forefront of steel production research and development (R&D), having 10 research centres worldwide.

Figure 2: Ceramic cup reconstruction. Source: ArcelorMittal.

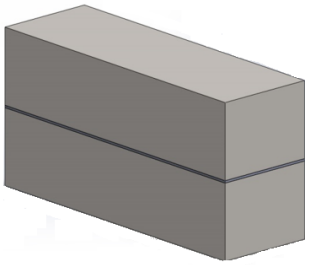

Figure 3: Proposed assembly of brick-mortar-brick. Source: ArcelorMittal.

The basic oxygen steelmaking is one of the major available methods for steel production. The process starts at the Blast Furnace (BF), a large countercurrent metallurgical furnace where, at very high temperatures, the iron ore is reduced and transformed into hot metal. The hot metal is the feed material for steel production, which has to be further processed after its extraction from the BF. Alongside with hot metal, the by-product known as slag is obtained inside the BF, which agglutinates the gangues of ore and the ashes of coal.

Provided that the temperature inside the BF reaches 1500°C, they are built using specific concrete refractories, which are able to withstand the extreme heat environment. Although their specific design may vary significantly, their most general characteristics are shared among all Blast Furnaces. Some of them have an additional protection layer, known as the ceramic cup. It is composed of refractory bricks sticked by joints made with castables, which are unshaped refractory materials. The ceramic cup is the innermost layer of the hearth wall located as shown in Fig. 1, only separated from the hot metal and slag by a thin castable protective lining. Outwards in the wall, a layer constructed with large carbon blocks separates the ceramic cup from the environment, increasing insulation. These carbon blocks are not joined together and can slide freely over each other.

Experimentation is very difficult due to the extreme heat environment, which motivates the industrial interest in the assessment of the thermo-mechanical behaviour of the refractory materials composing the BF by means of numerical simulation. For the ceramic cup simulation, this would require to consider both the castable joints and the bricks as different materials. Due to the number of bricks and the size of the joints (see Fig. 2), it would be computationally unfeasible .

The main goal proposed by the ArcelorMittal company was to study the optimal equivalent thermo-mechanical model for a brick-mortar-brick assembly (see Fig. 3). Two different alternatives were originally proposed for this 139 ESGI:

1. To consider an equivalent contact law among bricks instead of considering

the castable material at the joints.

2. To consider a homogenized equivalent material to the brick-mortar-brick assembly.

In addition, the company specifically wanted to analyze the feasibility of using open source-code software instead of a commercial package like ANSYS, which is currently used at ArcelorMittal. With this purpose, Code Aster was chosen to be compared with ANSYS.

Provided that the main goal is to ensure a simplification of the mathematical models to be solved, the alternative considering non-linear contact laws between bricks was disregarded in favour of the homogenization one. Consequently, the following work aims to find an equivalent elastic law for the brick-mortar-brick assembly by means of homogenization procedures.

There are many works in the bibliography related to homogenization tecniques for masonry constructions made up of bricks, with and without mortar, for linear and non-linear behaviour laws [4, 6, 8, 7]. In the literature, there is a body of work that concludes that ceramic materials, as the refractory concretes, behave as viscoplastic materials at high temperatures (see, for example, [9]). Here, we follow the technique used in [8] for linear elastic mortarless walls. It considers an equivalent material, whose elastic properties are found using basic tests posed on a representative unit cell of the wall.

In Section 2, we describe the methodology to characterize the homogenized equivalent material, based on a series of numerical tests on a unit cell domain. Thereafter, the obtained numerical results are presented in Section 3. Finally, in Section 4, we test the equivalent material on a configuration considering several bricks, comparing the displacements when using different properties for brick and mortar and the homogenized material properties instead.

2. Methodology

Following the second alternative proposed by ArcelorMittal, the problem is to find a homogenized constitutive law for the brick-mortar-brick assembly as depicted in Fig. 3. Nevertheless, a careful analysis of the ceramic cup wall led to the conclusion that the initially proposed assembly is not a representative set of the ceramic cup, in the sense that it does not constitute an element that is repeated in all directions.

Instead, we propose to consider a *unit cell* element as shown in Fig. 4, which verifies geometrical symmetry in all directions of the ceramic cup. This means that a good characterization of the mechanical response of this element can be extrapolated to the entire structure, which is the desired goal. The considered brick dimensions are $10 \times 10 \times 40$ cm whereas the mortar joints have a thickness of 12 mm.

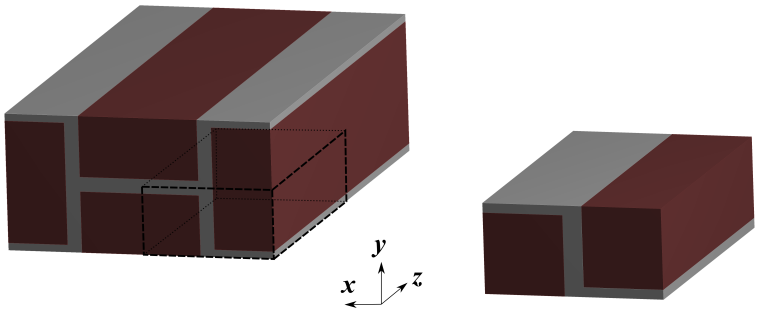

(a) Unit cell. (b) RUC.

Figure 4: Reduced unit cell (RUC) domain.

Thereby, inspired by the experimental tests that are usually performed to assess the elastic response of materials (see [5]), we propose a methodology that starts with the assumption that the homogenized material has a linear response to load. This response may be dependent on the direction, i.e., it could be an anisotropic behaviour. Then, the components of the strain tensor $\boldsymbol{\varepsilon}$ are related to those of the symmetric linearized stress tensor $\boldsymbol{\sigma}$ by the *compliance matrix* $[\mathbf{S}]$:

$$\begin{pmatrix} \varepsilon_{11} \\ \varepsilon_{22} \\ \varepsilon_{33} \\ 2\varepsilon_{23} \\ 2\varepsilon_{13} \\ 2\varepsilon_{12} \end{pmatrix} = \begin{pmatrix} S_{11} & S_{12} & S_{13} & S_{14} & S_{15} & S_{16} \\ S_{21} & S_{22} & S_{23} & S_{24} & S_{25} & S_{26} \\ S_{31} & S_{32} & S_{33} & S_{34} & S_{35} & S_{36} \\ S_{41} & S_{42} & S_{43} & S_{44} & S_{45} & S_{46} \\ S_{51} & S_{52} & S_{53} & S_{54} & S_{55} & S_{56} \\ S_{61} & S_{62} & S_{63} & S_{64} & S_{65} & S_{66} \end{pmatrix} \begin{pmatrix} \sigma_{11} \\ \sigma_{22} \\ \sigma_{33} \\ \sigma_{23} \\ \sigma_{13} \\ \sigma_{12} \end{pmatrix}. \tag{1}$$

If we denote as $\{\boldsymbol{\sigma}\}$ and $\{\boldsymbol{\varepsilon}\}$ the 6-component vectors of stress and strain, expression (1) can be recasted in compact form as:

$$\{\boldsymbol{\varepsilon}\} = [\mathbf{S}]\{\boldsymbol{\sigma}\}.$$

It can be shown that only 21 components of $[\mathbf{S}]$ need to be actually computed, provided that it is a symmetric matrix. Nevertheless, we propose to compute all 36 of them in order to check this assertion. With this purpose, we pose a system composed of 36 equations that arise from solving 6 independent stress states at the unit cell, defined as uniaxial compression or shear tests. The components of the *average stress* and *strain* vectors are computed by:

$$\{\overline{\boldsymbol{\sigma}}\}_i = \frac{1}{\mathrm{Vol}(\Omega)} \int_\Omega \{\boldsymbol{\sigma}\}_i \, dV, \qquad i \in \{1, 2, \ldots, 6\},$$

$$\{\overline{\boldsymbol{\varepsilon}}\}_i = \frac{1}{\mathrm{Vol}(\Omega)} \int_\Omega \{\boldsymbol{\varepsilon}\}_i \, dV, \qquad i \in \{1, 2, \ldots, 6\},$$

with Ω being the unit cell and Vol(Ω) its volume.

Thus, for test k, we compute the average stress and strain tensors in vector form, denoted as $\{\overline{\boldsymbol{\sigma}}\}^k$ and $\{\overline{\boldsymbol{\varepsilon}}\}^k$, respectively. Then, we assemble the corresponding equation i, with $i \in \{1, \ldots, 6\}$, using (1):

$$\sum_{j=1}^{6} S_{ij} \{\overline{\boldsymbol{\sigma}}\}_j^k = \{\overline{\boldsymbol{\varepsilon}}\}_i^k, \tag{2}$$

giving 6 equations for each test. Therefore, for the 6 tests we obtain the desired 36 equations. These will uniquely determine matrix [**S**] if the average stress and strain tensors are linearly independent for the designed tests.

To perform the numerical tests, we assume that both the brick and the mortar behave as linear elastic materials with the properties shown in Table 1. These are not measured values, but are consistent with the data available in the bibliography, as the castable used in the joints is expected to be much less stiff than the refractory brick, with its Young's modulus (E) being more than 100 times smaller.

2.1. Mathematical models on the unit cell

In order to assess the elastic behaviour of the unit cell, we propose to solve numerically the usual 6 mechanical tests: 3 in traction/compression and 3 in shear (see [5]). Both the castable mortar and the refractory brick are assumed to be isotropic linear materials, characterized with the properties shown in Table 1.

2.1.1 Compression tests

In the compression tests, the material is subjected to loads that are pointing in opposite directions. Provided that the displacement on the boundary is not known *a priori*, we choose a subdomain of the unit cell on which we can use symmetry boundary conditions to constrain the displacement. In this fashion, displacement is not fully imposed on any boundary. Thus, we only consider the piece of the unit cell shown in Fig. 4, corresponding to an eighth of the complete unit cell. We denote this reduced domain as Reduced Unit Cell (RUC).

	E (Pa)	ν
Refractory brick	1.0e9	0.2
Castable mortar	1.0e7	0.2

Table 1: Material properties.

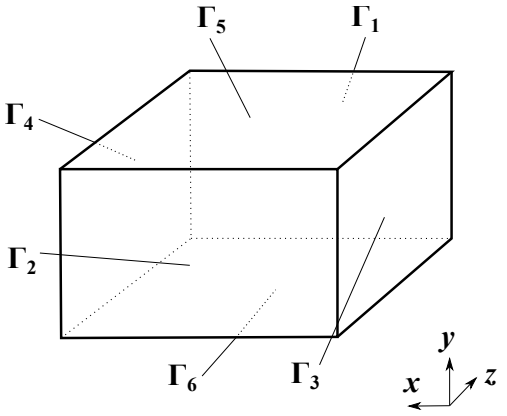

Figure 5: Boundary labels used for the numerical tests.

Let us denote the RUC as Ω, whose boundary Γ is split in Γ_n and Γ_s, such that $\Gamma = \overline{\Gamma}_n \cup \overline{\Gamma}_s$. Then, for the compression tests, we propose to find the displacement $\mathbf{u}(\mathbf{x})$ such that:

$$\begin{cases} -\mathrm{div}(\boldsymbol{\sigma}(\mathbf{u})) = \mathbf{0}, & \text{in } \Omega, \\ \boldsymbol{\sigma}(\mathbf{u}) = \lambda \mathrm{tr}(\boldsymbol{\varepsilon}(\mathbf{u}))\mathbf{I} + 2\mu\boldsymbol{\varepsilon}(\mathbf{u}), & \\ \boldsymbol{\sigma}(\mathbf{u})\mathbf{n} = \mathbf{g}, & \text{on } \Gamma_n, \\ \mathbf{u}\cdot\mathbf{n} = 0,\ \boldsymbol{\sigma}_t(\mathbf{u}) = \mathbf{0}, & \text{on } \Gamma_s. \end{cases} \tag{3}$$

The function $\mathbf{g}$ is the load applied on the boundary of the unit cell and varies at each of the compression tests. With $\mathbf{n}$ we denote the exterior unit normal vector, whereas $\boldsymbol{\sigma}_t$ is the tangential stress vector, i.e., the projection of the stress tensor in the tangent plane to the boundary. Moreover, with λ and μ we denote the *Lamé parameters*. These are related with the Young's modulus and the Poisson's ratio through

$$\lambda = \frac{E\nu}{(1-2\nu)(1+\nu)}, \qquad \mu = \frac{E}{2(1+\nu)}.$$

Note that both λ and μ depend on the material point $\mathbf{x}$, as the properties of the brick and the castable mortar are considered to be different. For clarity purposes, we use the labels shown in Fig. 5 to denote the faces that compose the boundary of the unit cell. Then, due to the position of the RUC with respect to the complete unit cell (see Fig. 4), we consider the symmetry boundary to be $\Gamma_s = \Gamma_1 \cup \Gamma_4 \cup \Gamma_5$.

Test 1: Compression stress state along the y axis. It is well known (see e.g. [3]) that to obtain this compression stress state in the unit cell it is enough to apply the same load on both the upper and lower faces of the domain. In the RUC, as shown in Fig. 6a, it suffices to consider:

$$\mathbf{g} = \begin{cases} (0, 1e6, 0)^t, & \text{on } \Gamma_6, \\ \mathbf{0}, & \text{on } \Gamma_2 \cup \Gamma_3. \end{cases}$$

Test 2: Compression stress state along the x axis. Following the same procedure, the load is applied on the faces with their normal vectors aligned with the x axis. Thus, as depicted in Fig. 6b we set:

$$\mathbf{g} = \begin{cases} (1e6, 0, 0)^t, & \text{on } \Gamma_3, \\ \mathbf{0}, & \text{on } \Gamma_2 \cup \Gamma_6. \end{cases}$$

Test 3: Compression stress state along the z axis. Analogously, to generate a stress state in the z axis we set:

$$\mathbf{g} = \begin{cases} (0, 0, 1e6)^t, & \text{on } \Gamma_2, \\ \mathbf{0}, & \text{on } \Gamma_3 \cup \Gamma_6, \end{cases}$$

as shown in Fig. 6c.

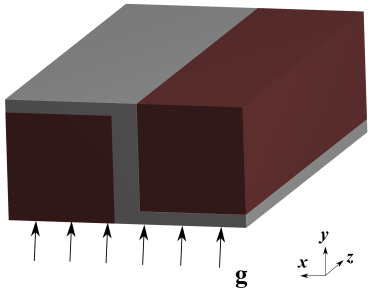

(a) Test 1: Compression on the y axis.

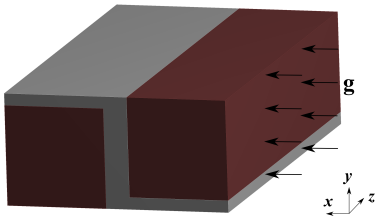

(b) Test 2: Compression on the x axis.

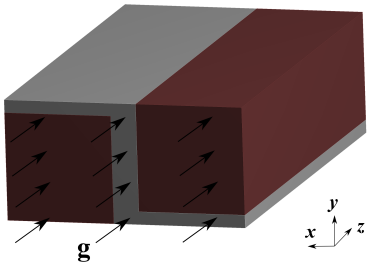

(c) Test 3: Compression on the z axis.

Figure 6: Loads applied in the compression tests.

2.1.2 Shear tests

In addition to the three compression tests, we need to solve three shear tests. For these shear tests, it is not possible to use symmetry conditions on the RUC chosen for the previous tests, as the loads that are to be applied do not satisfy it. Nonetheless, for each of the three shear stress states we can choose a new RUC that enables to set a symmetry condition on a face of the unit cell, as shown in Figs. 7, 8 and 9.

Unfortunately, this symmetry condition only constrains displacements in the normal direction to the symmetry face. Thus, the problem in the RUC does not have a unique solution. This is due to the kernel of the $\boldsymbol{\varepsilon}$ operator being the space of rigid motions of Ω (denoted as $\mathrm{RM}(\Omega)$), which are not restricted by the boundary conditions. For more details on this difficulty, we refer to [2, Chapter 9]. In order to obtain a unique solution, we set $\mathbf{u} = \mathbf{0}$ at the nodes corresponding to an element face situated close to the axis of the rotation generated by the shear state. Then, the only $\boldsymbol{\omega} \in \mathrm{RM}(\Omega)$ that satisfies this boundary condition is $\boldsymbol{\omega} \equiv \mathbf{0}$. We denote this element face as Γ_d.

Consequently, we have that $\Gamma = \overline{\Gamma}_s \cup \overline{\Gamma}_n \cup \overline{\Gamma}_d$ for the shear tests. Thus, the problem is to find the $\mathbf{u}(\mathbf{x})$ s.t.:

$$\begin{cases} -\mathrm{div}(\boldsymbol{\sigma}(\mathbf{u})) = \mathbf{0}, & \text{in } \Omega, \\ \boldsymbol{\sigma}(\mathbf{u}) = \lambda \mathrm{tr}(\boldsymbol{\varepsilon}(\mathbf{u}))\mathbf{I} + 2\mu\boldsymbol{\varepsilon}(\mathbf{u}), & \\ \boldsymbol{\sigma}(\mathbf{u})\mathbf{n} = \mathbf{g}, & \text{on } \Gamma_n, \\ \mathbf{u}\cdot\mathbf{n} = 0, \boldsymbol{\sigma}_t(\mathbf{u}) = \mathbf{0}, & \text{on } \Gamma_s, \\ \mathbf{u} = \mathbf{0}, & \text{on } \Gamma_d. \end{cases} \tag{4}$$

For the sake of simplicity, we use the labels shown in Fig. 5 for the three different RUCs that we consider, using that each of them will have six faces which are identically oriented as in the sketch.

Test 4: Shear stress state in the xz plane. The RUC is chosen as depicted in Fig. 7, which corresponds to the bottom half of the unit cell. The symmetry condition is applied on the top face, i.e., $\Gamma_s = \Gamma_5$. Then, the element face where the condition $\mathbf{u} = \mathbf{0}$ is imposed is located on the bottom face of the RUC, which means that $\Gamma_d \subset \Gamma_6$. The load $\mathbf{g}$ used to generate this shear stress state is set as

$$\mathbf{g} = \begin{cases} (-1e6, 0, 0)^t, & \text{on } \Gamma_1, \\ (1e6, 0, 0)^t, & \text{on } \Gamma_2, \\ (0, 0, 1e6)^t, & \text{on } \Gamma_3, \\ (0, 0, -1e6)^t, & \text{on } \Gamma_4, \\ \mathbf{0}, & \text{on } \Gamma_6 - \Gamma_d. \end{cases}$$

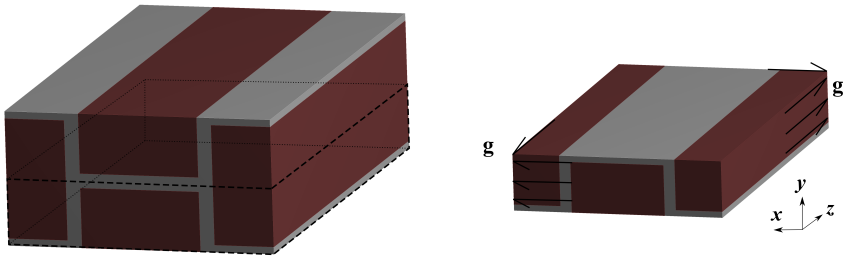

(a) RUC. (b) Applied load.

Figure 7: Test 4. Shear stress in the xz plane.

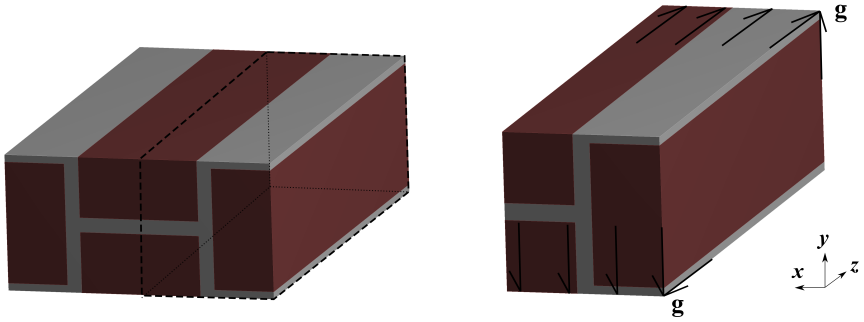

(a) RUC. (b) Applied load.

Figure 8: Test 5. Shear stress in the yz plane.

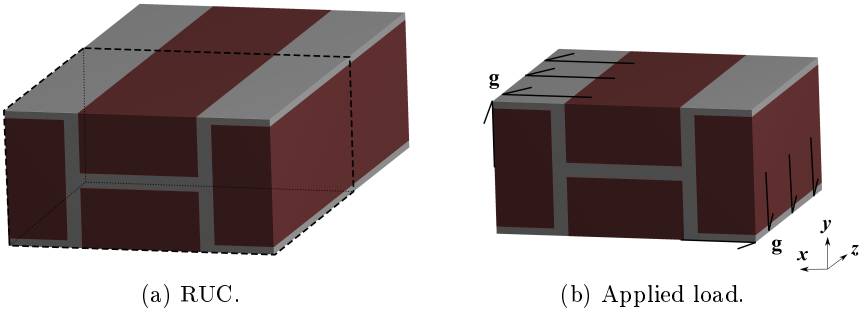

(a) RUC. (b) Applied load.

Figure 9: Test 6. Shear stress in the xy plane.

Test 5: Shear stress state in the yz plane. Similarly, to obtain a shear stress state in the plane yz, the RUC is taken as depicted in Fig. 8, which corresponds to the right half of the unit cell. Thus, we have that $\Gamma_s = \Gamma_4$ and $\Gamma_d \subset \Gamma_3$. The load $\mathbf{g}$ is defined as

$$\mathbf{g} = \begin{cases} (0, 1e6, 0)^t, & \text{on } \Gamma_1, \\ (0, -1e6, 0)^t, & \text{on } \Gamma_2, \\ (0, 0, 1e6)^t, & \text{on } \Gamma_5, \\ (0, 0, -1e6)^t, & \text{on } \Gamma_6, \\ \mathbf{0}, & \text{on } \Gamma_3 - \Gamma_d. \end{cases}$$

Test 6: Shear stress state in the xy plane. Analogously, to consider a stress state in the plane xy, the RUC is taken as the front half of the unit cell, as shown in Fig. 9. Therefore, the symmetry boundary is $\Gamma_s = \Gamma_1$ and $\Gamma_d \subset \Gamma_2$. The applied load $\mathbf{g}$ is set as follows:

$$\mathbf{g} = \begin{cases} (0, -1e6, 0)^t, & \text{on } \Gamma_3, \\ (1e6, 0, 0)^t, & \text{on } \Gamma_5, \\ (0, 1e6, 0)^t, & \text{on } \Gamma_4, \\ (-1e6, 0, 0)^t, & \text{on } \Gamma_6, \\ \mathbf{0}, & \text{on } \Gamma_2 - \Gamma_d. \end{cases}$$

3. Numerical results

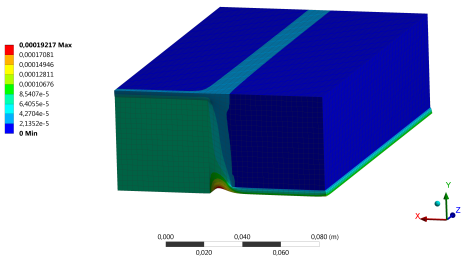

(a) Displacement.

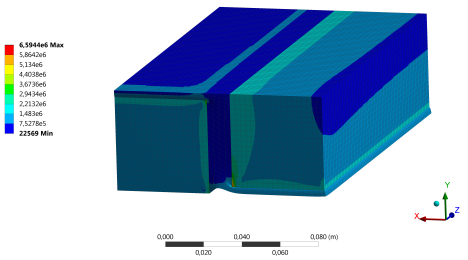

(b) Von Mises stress.

Figure 10: Test 1.

The proposed six tests are solved using both ANSYS Mechanical and Code-Aster. Results show that there is a good level of agreement among both the commercial and the open source code. The contours of displacement and von Mises stress norm obtained in the compression tests are shown in Figs. 10–12, whereas the computed contours in the shear tests are depicted in Figs. 13–15.

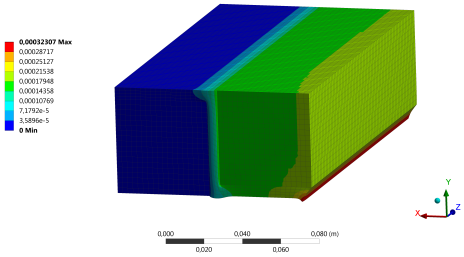

(a) Displacement.

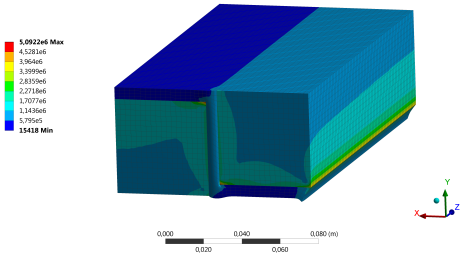

(b) Von Mises stress.

Figure 11: Test 2.

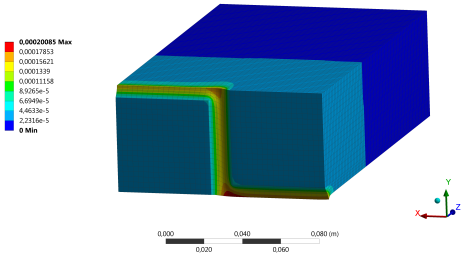

(a) Displacement.

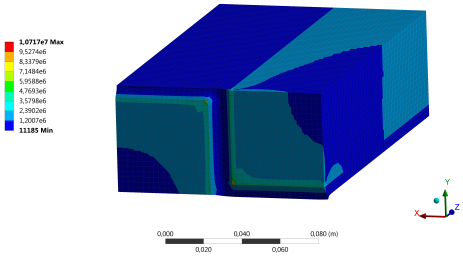

(b) Von Mises stress.

Figure 12: Test 3.

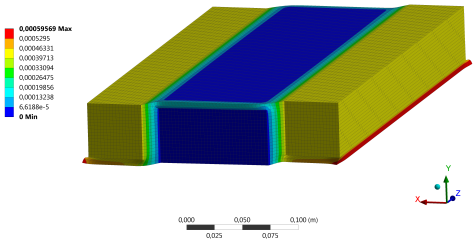

(a) Displacement.

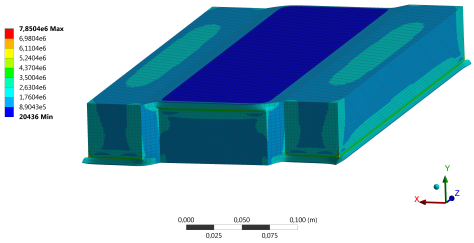

(b) Von Mises stress.

Figure 13: Test 4.

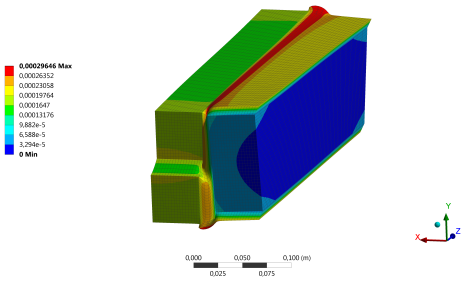

(a) Displacement. (b) Von Mises stress.

Figure 14: Test 5.

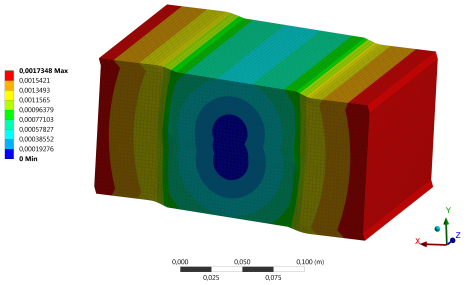

(a) Displacement. (b) Von Mises stress.

Figure 15: Test 6.

The computed average stresses and strains are used to obtain [**S**] via the solution of the linear system arising from eqns. (2). The linear system has 36 equations and unknowns, and was solved using the symbolic math toolbox available in MATLAB. The obtained matrix is the following:

$$[\mathbf{S}] = 1e-9 \begin{pmatrix} \mathbf{1.70} & \mathbf{-1.60e-1} & \mathbf{-4.72e-2} & -8.28e-13 & 1.90e-9 & -4.26e-10 \\ \mathbf{-1.60e-1} & \mathbf{1.63} & \mathbf{-4.69e-2} & -5.56e-11 & -4.54e-10 & -1.13e-9 \\ \mathbf{-4.72e-2} & \mathbf{-4.69e-2} & \mathbf{2.61e-1} & -5.49e-11 & -2.75e-11 & -5.28e-9 \\ 6.30e-4 & 1.24e-3 & 7.50e-4 & \mathbf{3.84e-1} & -1.57e-8 & 8.25e-9 \\ -2.15e-3 & -6.17e-3 & 2.52e-3 & 2.68e-8 & \mathbf{4.28e-1} & 5.76e-6 \\ -1.83e-3 & -2.97e-1 & 2.26e-3 & 4.46e-9 & -1.57e-8 & \mathbf{6.78e-1} \end{pmatrix}$$

Leading order entries in the matrix have been highlighted for clarity purposes. There is a problem with the 3×3 block at the bottom left, as some entries of the same order as the leading order ones appear. Furthermore, these show no symmetry with the top right block. As discussed previously, the resulting matrix must be symmetric, which indicates that there is an error in the performed computations. This puts into question the symmetry assumption

used for the compression tests. Nevertheless, the remaining entries outside of the problematic block behave as expected, preserving the required symmetry.

For an orthotropic material, the compliance matrix in a basis perpendicular to the symmetry planes satisfies:

$$[\mathbf{S}] = \begin{pmatrix} 1/E_1 & -\nu_{12}/E_1 & -\nu_{13}/E_1 & 0 & 0 & 0 \\ -\nu_{21}/E_2 & 1/E_2 & -\nu_{23}/E_2 & 0 & 0 & 0 \\ -\nu_{31}/E_3 & -\nu_{32}/E_3 & 1/E_3 & 0 & 0 & 0 \\ 0 & 0 & 0 & 1/\mu_{12} & 0 & 0 \\ 0 & 0 & 0 & 0 & 1/\mu_{13} & 0 \\ 0 & 0 & 0 & 0 & 0 & 1/\mu_{23} \end{pmatrix}.$$

Thus, if a material is orthotropic, it can be fully characterised by 9 independent material constants, which can be computed from the compliance matrix. Note that if we ignore the problematic block and assume that is equal to zero, the computed compliance matrix is very similar to the expected one for an orthotropic material. In that case, the material coefficients are:

$$\begin{array}{lll} E_1 = 5.88e8 \text{ Pa}, & E_2 = 6.13e8 \text{ Pa}, & E_3 = 3.83e9 \text{ Pa}, \\ \nu_{12} = 9.41e-2, & \nu_{13} = 2.78e-2, & \\ \nu_{21} = 9.82e-2, & \nu_{23} = 2.88e-2, & \\ \nu_{31} = 1.81e-1, & \nu_{32} = 1.80e-1, & \\ \mu_{12} = 1.48e8 \text{ Pa}, & \mu_{13} = 2.34e8 \text{ Pa}, & \mu_{23} = 2.62e8 \text{ Pa}. \end{array} \tag{5}$$

These coefficients closely resemble the ones of a transversely isotropic material (see [1]). Note that the behaviour is clearly different in the xy plane, where there are closed joints, as opposed to the behaviour in the z direction, along which the mortar joints are aligned.

4. Homogenized material

The compliance matrix $[\mathbf{S}]$, computed through the numerical tests, characterizes the behaviour of the anisotropic linear material. This anisotropic material should describe the mechanical response of a homogenized assembly of unit cells, i.e., a wall similar to the ceramic cup. If the methodology is valid, then the response considering the different material properties for brick and mortar should be similar to the response of the homogenized material.

To define the homogenized material we use the coefficients gathered in (5). Then, 16 unit cells in a 4×4 arrangement are used to construct a wall, as depicted in Fig. 16. The domain can be defined as:

$$\Omega = [0, 0.896] \times [0, 0.448] \times [0, 0.4].$$

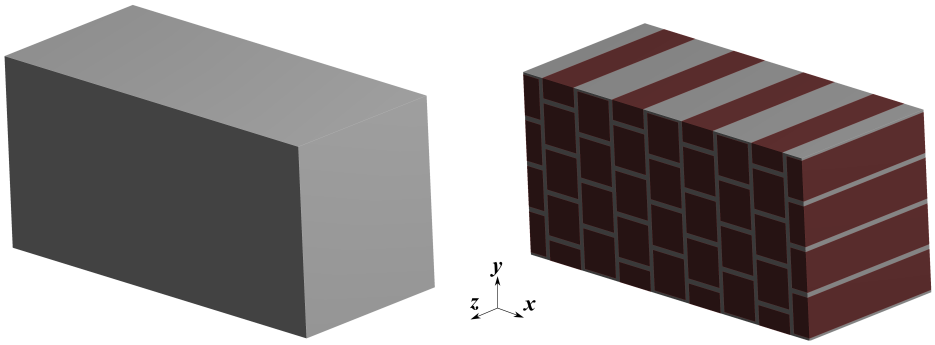

(a) Homogenized material. (b) Non-homogenized assembly.

Figure 16: Assembly of 16 unit cells.

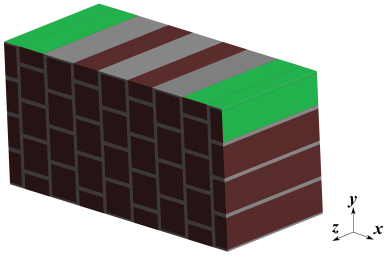

Figure 17: Boundary Γ_{n1}.

The wall is subjected to a pressure $p = 1e6$ Pa on the boundary Γ_{n1}, which corresponds with the two top corners. This boundary, shown in Fig. 17, is defined as follows:

$$\begin{aligned}\Gamma_{n1} = &\{(x,y,z) \in \Omega : y = 0.448, x < 0.224\} \\ &\cup \{(x,y,z) \in \Omega : y = 0.448, x > 0.672\} \\ &\cup \{(x,y,z) \in \Omega : x = 0, y > 0.336\} \\ &\cup \{(x,y,z) \in \Omega : x = 0.896, y > 0.336\}.\end{aligned}$$

In addition, we set $\mathbf{u} = \mathbf{0}$ at Γ_d:

$$\Gamma_d = \{(x,y,z) \in \Omega : y = 0\},$$

which corresponds with the bottom of the wall.

On the remainder of the boundary we set that $\boldsymbol{\sigma}\mathbf{n} = \mathbf{0}$. Solving the problem for both the homogenized material and considering the different properties for brick and mortar, we obtain the displacements shown in Fig. 18. The maximum value of the displacement for the homogenized material is around 0.67 mm, whereas considering the two different materials is 0.71 mm. Despite these differences in the computed maximums, it is clear that the response of

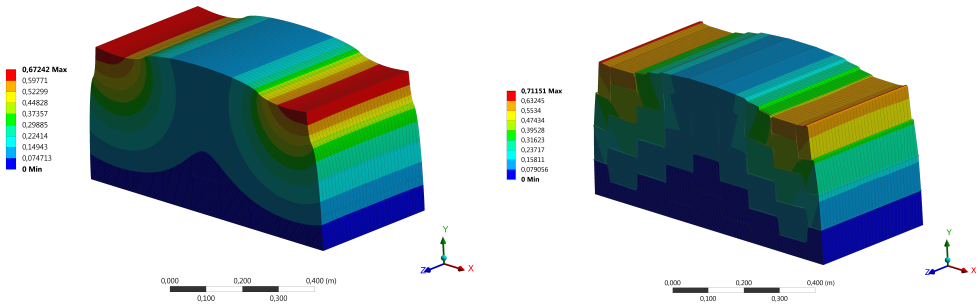

(a) Homogenized material. (b) Non-homogenized materials.

Figure 18: Contours of displacement (mm).

the homogenized assembly and the wall considering both materials is quite similar.

Using the proposed methodology, albeit with a small loss in accuracy, a much faster solution of the model can be achieved. This is mainly due to not having to mesh every mortar joint individually, which leads to extremely fine meshes. Thus, a much coarser mesh can be used, which is crucial in order to simulate the entire ceramic cup.

5. Conclusions and Future Work

The proposed methodology has shown promising results as the performed tests were successfully used to predict the anisotropic behaviour of the brick and mortar assembly that composes the ceramic cup of a blast furnace.

Nevertheless, the obtained compliance matrix [**S**] has clear shortcomings. Namely, the entries in the matrix that neither verify symmetry nor are related with usual anisotropic behaviour seem to be coming from the assumption that the symmetry conditions hold for an heterogeneous material. Future work aims to improve the methodology in order to eliminate said errors. Moreover, it has to be extended to the thermo-mechanical case, where the thermal problem needs to be considered as well as the temperature dependency of the material properties.

Real refractory materials under high temperatures do not behave as linear elastic materials. In the future, this should be taken into consideration in order to obtain more accurate descriptions of the homogenized material.

Experiments should be used to obtain the correct mechanical properties of both castable mortar and refractory brick. In addition, the numerical results should be also experimentally validated.

Acknowledgements This work was partially supported by FEDER and Xunta de Galicia funds under the ED431C 2017/60 grant, by the Ministry of Economy, Industry and Competitiveness through the Plan Nacional de I+D+i (MTM2015-68275-R), the grant BES-2016-077228 and the project Reduced Order Modelling, Simulation and Optimization of Coupled Systems (ROMSOC), with ID 765374 on the topic MSCA-ITN-2017 - Innovative Training Networks (European Industrial Doctorates).

The authors would also like to acknowledge ArcelorMittal and personally thank Alejandro Lengomín for their help.

References

[1] Allan F Bower. *Applied mechanics of solids.* CRC press, 2009.

[2] Susanne Brenner and Ridgway Scott. *The mathematical theory of finite element methods,* volume 15. Springer Science and Business Media, 2007.

[3] Philippe G Ciarlet. *Three-dimensional elasticity,* volum 20. Elsevier, 1988.

[4] Alain Gasser, Kristin Terny-Rebeyrotte, and Philippe Boisse. Modelling of joint effects on refractory lining behaviour. *Proceedings of the Institution of Mechanical Engineers, Part L: Journal of Materials: Design and Applications*, 218(1):19-28, 2004.

[5] Jean Lemaitre and Jean-Louis Chaboche. *Mechanics of solid materials.* Cambridge university press, 1994.

[6] Paulo B Lourenço, Alberto Zucchini, Gabriele Milani, and Antonio Tralli. Homogenisation approaches for structural analysis of masonry buildings. 2006.

[7] NJ Mathieu, Karam Sab, and SA Zaïmi. An enhanced homogenization approach for masonry structures with compressible joints. application to hearth thermomechanical computations. *International Journal for Numerical and Analytical Methods in Geomechanics*, 36(9):1102-1124, 2012.

[8] TMH Nguyen, E Blond, A Gasser, and T Prietl. Mechanical homogenisation of masonry wall without mortar. *European Journal of Mechanics-A/Solids*, 28(3):535-544, 2009.

[9] Alberto Zucchini and Paulo B Lourenço. A micro-mechanical homogenisation model for masonry: Application to shear walls. *International Journal of Solids and Structures*, 46(3-4):871-886, 2009.

Acknowledgements

The Scientific Committee wishes to thank to the company speakers, the academic coordinators and the researchers of each working team for their invaluable contributions to the scientific success of the 139 European Study Group with Industry.

This 139 ESGI was framed as activity in ITMATI in collaboration with math-in. The COST Action TD1409, Mathematics for Industry Network (MI-NET) has co-organized and co-funded this event. The ESGI was also co-funded by the Ministry of Economy, Industry and Competitiveness–State Research Agency with the nº of reference MTM2016-81745-REDT through the Thematic Network RTmath-in and via the Strategic Network in Mathematics with the nº of reference MTM2016 -81711- REDE, granted within the call "Networks of Excellence" 2016; by the Regional Ministry of Culture, Education and University Planning of the Regional Government of Galicia through the Technological Network of Industrial Mathematics (TMATI Network); by the agreement that ITMATI has with this Regional Ministry; and by ROMSOC project, financed by the EU within the Horizon 2020 Research and Innovation Programme under the Marie-Skłodowska-Curie grant agreement No 765374. Because of that, we want to express our gratitude to all of them. We would also like to thank to the Faculty of Mathematics of the University of Santiago de Compostela which held the 139 ESGI.

Finally, we would also like to express our gratitude to Andrés Prieto Aneiros, Associate Professor in the Department of Mathematics of the Faculty of Computer Science at University of A Coruña and Affiliated Researcher to ITMATI, Yago Casal Nogueira, Technology Translator of math-in, Martín Sanjurjo García, Transfer Manager and Assistant Technology Translator at ITMATI and Raluca Silvana Tomoni, Technology Transfer and Innovation Manager at ITMATI, whose meticulous work and dedication have contributed to the success of this 139 European Study Group with Industry.

Solidification and mechanical coupling in the propagation of microcracks

Simplified Modeling of Brazing Furnaces

Order Reduction on Dynamic Systems using Machine Learning

Predictive maintenance in a pellet production factory

Equivalent thermo-mechanical model for ceramic cups

Universidade Vigo

USC UNIVERSIDADE DE SANTIAGO DE COMPOSTELA

UNIVERSIDADE DA CORUÑA